Quaternary Science Reviews
June 2023, Volume 310 Pages 108114 (17p.)
https://doi.org/10.1016/j.quascirev.2023.108114
https://archimer.ifremer.fr/doc/00838/94978/

Lunar nodal tidal cycle influences on the input of coarse sediments during the last glaciation in the deep South China Sea

Zhao Hongchao [1], Liu Zhifei [1, *], Zhao Yulong [1], Wu Jiawang [1], Colin Christophe [2]

[1] State Key Laboratory of Marine Geology, Tongji University, Shanghai, 200092, China
[2] Université Paris-Saclay, CNRS, GEOPS, Orsay, 91405, France

* Corresponding author : Zhifei Liu, email address : lzhifei@tongji.edu.cn

Abstract :

Cross-slope transport of coarse sediments is thought to be dominated by gravity-flow or hyperpycnal-flow processes triggered by hydrodynamic events. However, whether long-term non-event hydrological processes can affect longitudinal transport is still unclear. Here, high-resolution (1 mm) X-ray fluorescence core scanning combined with coarse-fraction observation has been conducted on a laminated sequence (dated as last glacial 14.3–20.8 cal ka BP) of Core MD05-2892 in the South China Sea. The laminae show interbedded millimeter-scale dark and light layers. Dark layers are distinguished by coarse-grained (sand-containing clayey silt) sediments rich in Ca, Zr, and Si, whereas light layers are characterized by fine-grained (silty clay) deposits rich in K, Ti, and Fe. Accordingly, Zr/K and Si/K ratios are used to indicate lamina occurrences, and the ratios are well correlated to grayness. Spectral analyses of the ratios and grayness all present a persistent ~18.6-yr cycle, which is interpreted as the lunar nodal tidal cycle. This signal in laminae could be related to remobilization of coarse sediments via mean high-water-line variations driven by the lunar nodal tide during the last glacial sea-level lowstand. Coarse sediments were more likely transported from the shelf break via suspended-load-dominated hyperpycnal flow to the slope to form dark layers during periods of strengthened tidal activity, while fine sediments were dispersed via hemipelagic transport to form light layers during periods of weakened tidal activity. Our study highlights for the first time that the lunar nodal tide could periodically trigger the transport of coarse sediments from the shelf to the deep sea.

Highlights

► First observation of lunar nodal tidal cycle deposition in the deep South China Sea. ► Interbedding laminae represent hyperpycnal-flow and hemipelagic transport processes. ► Lunar nodal tide could periodically trigger cross-slope transport of coarse sediments.

Keywords : Lunar nodal tidal cycle, Laminae, Hyperpycnal flow, X-ray fluorescence (XRF) core scanning, South China Sea

1. Introduction

The transport process of coarse sediments from the shelf to the deep sea is an important sedimentary dynamic process for understanding the global flux of continent-to-ocean sediment transfer. For example, this cross-slope transport dominates the burial of terrigenous plant debris in the deep sea, and such carbon sequestration over geological timescales would ultimately influence global climate via the regulation of the greenhouse gas (Liu et al., 2012; Lee et al., 2019). In addition, this cross-slope transport mainly works in forms of gravity flows or hyperpycnal flows (Zavala and Pan, 2018; Shanmugam, 2020). Regarding the triggering mechanism, such cross-slope transport is shown to be event-driven in most cases, such as typhoon-induced turbidity currents (Zhang et al., 2018), earthquake-triggered submarine landslides (Hsu et al., 2008), and flood-induced hyperpycnal flows (Nakajima, 2006). A few studies showed that periodic hydrodynamic processes, especially asymmetric reciprocal currents due to tidal activity, can also affect the cross-slope transport (Lintern et al., 2016; Hage et al., 2019). For example, a modern observation in the northwestern Ross Sea showed that downslope volume fluxes of high-density bottom currents were 2.5 times larger during spring tides than during neap tides (Padman et al., 2009), indicating the possibility that more materials were transported across the slope at spring tides than at neap tides. A modern observation in the northwestern Atlantic Ocean showed that strong gravity flows contributed to the transport of coarse sediments towards the deep sea in one or two tidal cycles in wintertime (Puig et al., 2013). Due to the limitation of observation time, these studies mainly monitored the signal of short-term tidal cycles (<14 days) on the high-density currents and gravity currents (Padman et al., 2009; Puig et al., 2013), indicating that short-term tidal cycles influence the sediment transport across the slope. However, it is unclear about how tidal

cycles would influence the longitudinal transport of sediments from a long-term scale perspective.

The main long-term tidal cycle is the lunar nodal cycle (Pugh, 1987). The lunar nodal cycle is caused by the rotation of nodal points between the lunar orbit and the solar orbit with a period of 18.6 yr (Pugh, 1987). Since tidal intensity on the Earth is mainly controlled by the lunar gravitational force, the lunar nodal cycle can cause periodic changes in tidal intensity (Kaye and Stuckey, 1973; Oost et al., 1993). It has been found that the mean high-water-line in the coastal zone of northeastern South America increased by 6 cm under the influence of the lunar nodal tidal cycle, resulting in an erosion of about 400 million tons of coastal sediments (Gratiot et al., 2008). The mean high-water-line in the southern South China Sea varies dramatically under the influence of the lunar nodal tidal cycle, with as high as 20 cm in the Gulf of Thailand and 2–8 cm offshore the Malay Peninsula and the Sumatra (Peng et al., 2019). Considering the strong erosion of tides assessed in northeastern South America, the lunar nodal tidal cycle possibly has a great impact on the erosion and cross-slope transport of sediments in the South China Sea. Under modern conditions, tide-eroded sediments accumulate usually in shallow continental shelf areas (Ta et al., 2002; Staub and Gastaldo, 2003; Tomkratoke et al., 2015). Accordingly, coastal sediments are unlikely to be remobilized across the broad Sunda Shelf (~800 km width) to the deep-sea slope under the lunar nodal tidal influence. During the last glacial sea-level lowstand, however, the paleo-shoreline was located near the present-day shelf break (Hanebuth et al., 2000, 2011; Voris, 2000; Sathiamurthy and Voris, 2006), resulting in coastal sediments close to the shelf break. On such a glacial land-sea morphology configuration, the coastal sediments were prone to be remobilized across the shelf break to the deep-sea slope under the effect of the lunar nodal tide. It has

been demonstrated that sediment inputs to the deep South China Sea from the extremely wide and exposed Sunda shelf were an order of magnitude larger in the last glaciation than in present time (Steinke et al., 2008). Such a glacial land-sea configuration makes the deep South China Sea a natural laboratory for studying the influence of the lunar nodal tidal cycle on the cross-slope transport of sediments.

In this study, Core MD05-2892 in the Sunda Slope of the southern South China Sea was analyzed by the high-resolution (1 mm) X-ray fluorescence (XRF) core scanning method in combination with microscopic observation of coarse fractions in typical samples to decipher the sedimentary characteristic during the last glacial sea-level lowstand and its reflected cross-slope transport mechanism. Our results indicate that the lunar nodal tide could periodically trigger the cross-slope transport of coarse sediments, which is an important transport mechanism of sediments on the Sunda Shelf during the last glaciation. To our knowledge, it is also the first report that the lunar nodal tide could induce a cyclic sedimentation in the deep sea via the hyperpycnal-flow transport from the shelf.

2. Material and Methods

2.1. Material

Core MD05-2892 (Calypso core; 6°06.12′ N, 110°40.71′ E; –1,183 m water depth) was retrieved from the lower Sunda Slope in the southern South China Sea during the MD147-Marco Polo Cruise in 2005 (Laj et al., 2005) (Fig. 1). The core is 29.0 m long and this study focuses on sediment sections of the upper 13.7 m. The lithology of the upper sections is dominated by olive gray homogeneous silty clay for the 0–3.6 m interval and dark gray laminated silty clay and clayey silt for the 3.6–13.7 m interval (Laj et al., 2005). The latter is characterized by millimeter-scale laminae, visually embodied as the

interbedding dark and light gray layers (Fig. 2). The grain size of dark-layer sediments (mainly as sand-containing clayey silt) is coarser than that of light-layer sediments (mainly as silty clay), and the contact boundary between dark and light layers is gradational by visual observation. Notably, Cores MD05-2893 (Casq core; 6°06.07′ N, 110°40.72′ E; –1,183 m water depth) and MD05-2892 are almost at the same location (Laj et al., 2005). Because of almost same locations of the two cores, the oxygen isotope stratigraphy of the two cores are compared to obtain oxygen isotope stratigraphic tie-points. These tie-points are useful to construct the age model of Core MD05-2892.

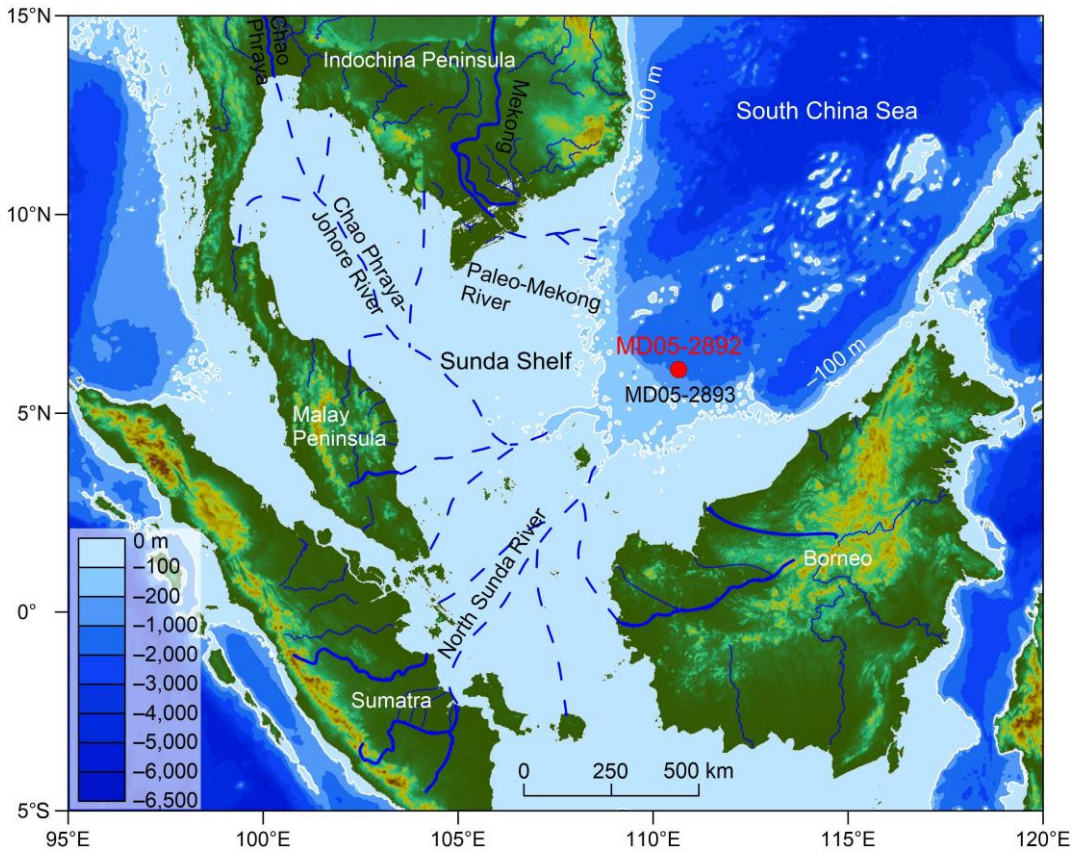

Fig. 1. Topography and bathymetry of the southern South China Sea showing the location of Core MD05-2892 (Calypso core). Cores MD05-2893 (Casq core) and MD05-2892 are almost at the same location (Laj et al., 2005). The present-day isobath of –100 m approximately depicts the paleo-shoreline during the last glaciation. The networking of paleo-river systems (dashed lines) during the last sea-level lowstand is shown (Molengraaff and Weber, 1921; Voris, 2000; Sathiamurthy and Voris, 2006).

All sediment sections (29.0 m) of Core MD05-2892 were scanned for XRF elements, and elemental data of the upper 13.7 m were used in this study. Photographs of the upper 13.7 m and their grayness values are useful for semi-quantitative identification of laminae. A total of 210 samples from the upper 13.7 m were sieved to examine the nature of coarse fractions (>63 μm grain size). Besides, planktonic foraminifera were picked from the coarse fractions for oxygen isotope analyses. Ten samples were selected for accelerator mass spectrometry radiocarbon (AMS ^{14}C) dating. The dating and oxygen isotope results were used together to construct an age model of Core MD05-2892.

2.2. Methods

XRF core scanning provides rapid, non-destructive, high-resolution, and semiquantitative records of the chemical composition on split sediment cores (Croudace et al., 2006; Richter et al., 2006). The principle of XRF is based on the excitation of electrons by incident X-rays (Richter et al., 2006, and references therein). For conventional XRF analysis, the fused or power samples need to be homogeneous, dry, and have a flat and smooth surface. After calculation of standard samples, conventional XRF analysis provides absolute element contents of sediment samples (Sang et al., 2022). The sum of absolute element contents is not a constant value, usually fluctuating between 90% and 110%. For XRF core scanning analysis, the split sediment core is characterized by an inhomogeneous, wet, and rough surface (Richter et al., 2006; Tjallingii et al., 2007). Due to the surface nature of sediment cores and no standard sample calculation, the XRF core scanner outputs semiquantitative datasets. The output datasets are expressed as element intensities in total counts (cnts) or counts per second (cps), which are proportional to the chemical concentrations (Tjallingii et al., 2007). Although element intensities mainly

depend on the element concentration, they are also influenced by the energy level of the X-ray source, the count time, and the physical properties of the sediment (Tjallingii et al., 2007, and references therein). For example, the total intensity of all elements in a deep-sea core is not constant-sum data, and its variations are related to changes in chemical composition and wet bulk density (Tjallingii et al., 2007). Without constant-sum constraints, variations of one certain element of XRF results are independent and not influenced by other elements' variations.

Two rounds of XRF core scanning were conducted on Core MD05-2892. First, it was performed on all core sections (29.0 m) with 1 cm resolution using an Avaatech XRF core scanner at the State Key Laboratory of Marine Geology, Tongji University. In order to better characterize elemental variations in millimeter-scale laminae, XRF core scanning with 1 mm resolution along with X-ray image collection was performed on the 3.6–13.7 m interval using an Itrax XRF core scanner at the Second Institute of Oceanography, Ministry of Natural Resources. Both XRF core scanning processes followed the same test protocol (Wu et al., 2013). Before measurement, the core surface was carefully flattened and covered with a special film (4-μm thickness). The parameters of the Avaatech instrument were set for 30-s exposure time, three voltage and current conditions including 10 kV and 0.2 mA for $_{13}$Al–$_{26}$Fe, 30 kV and 0.8 mA for $_{27}$Co–$_{42}$Mo, as well as 50 kV and 0.2 mA for $_{43}$Tc–$_{92}$U (Xie et al., 2014). The parameters of the Itrax instrument were set for 10-s exposure time, 60-kV voltage and 45-mA current for all elements. After measurement, the XRF core scanner outputted the chemical composition of sediments as element intensities in counts per second (cps). Although element intensities mainly depend on the element concentration of sediments, they are also influenced by instrument parameters (e.g., exposure time) and physical properties of the sediment (e.g., water

content and lithological inhomogeneity) (Tjallingii et al., 2007, and references therein). There is a systematic deviation between the results of two resolution tests, possibly due to the instrument parameter difference. We normalized the 1-cm resolution result using a linear fit to match the 1-mm resolution result (Supplementary Data Tables S1 and S2). After normalization, the element intensities of light elements (e.g., Si, atomic weight 28) are lower than those of heavy elements (e.g., Fe, atomic weight 56), which is possibly related to the response depth of elements to incoming X-ray radiation. The response depth is dependent on the wavelength of emitted radiation, itself related to atomic weight, and on the chemical composition of the matrix (Richter et al., 2006, and references therein). Although the detected area on the sediment surface is the same for each element, the response depth of each element is different. Accordingly, the detected volumes of heavy elements are larger than those of light elements, resulting in higher intensity values of heavy elements than those of light elements. In addition, the element intensities of light elements are prone to be influenced by the physical properties of the sediment. Therefore, the element intensities are output results under different influence factors, and each element intensity changes independently.

Grayness was extracted from core photos (Supplementary Data Photo package) using Python codes (Supplementary Data Text S1 and Python script). The codes were converted into a Python script and then placed in the same folder as the core photos. Run the script and input the core-photo name to open the photo. Then, click on the photo with the mouse and press the P letter to set three lines. One line was assigned at the core axis along the depth direction on the core photo. The other two lines are top and bottom on the core photo, respectively. Then, press Esc button and input depth values of the top and bottom on the script. After running the script, color signals (R, G, B) of the photos were

automatically extracted and converted into grayness values (Table S3). The conversion equation is grayness value = 0.3 × R + 0.59 × G + 0.11 × B (Hossain et al., 2018). Larger values represent lighter color. In addition, the thickness and depth positions of dark layers were obtained by manual statistics using core photos and X-ray images (Table S4).

Coarse fractions were observed using a stereomicroscopy and a scanning electron microscopy-energy spectroscopy analyzer (SEM-EDS). Before observation, bulk samples were dried at 40ºC for 24 h and then soaked in deionized water for 24 h. The soaked samples were sieved with a 63-μm sieve. After sieving, coarse fractions were collected and dried for preservation. General features of coarse fractions were observed by a stereomicroscopy, and then coarse fractions of typical samples were sprayed with gold and placed in a SEM-EDS instrument to analyze their morphological and elemental characteristics. Stereomicroscopy observation was done using a Zeiss Stereo Discovery binocular with magnification of 8–40 times; SEM observation was performed with a Tescan Mira3 field emission scanning electron microscope with parameters of 10–20 kV and 0° rotation angle. These analyses were performed at the State Key Laboratory of Marine Geology, Tongji University.

Oxygen isotope compositions ($\delta^{18}O$) were measured on *Globigerinoides ruber* (*G. ruber*) (250–360 μm size) using a Finnigan MAT 252 Mass Spectrometer at the State Key Laboratory of Marine Geology, Tongji University. Clean and intact *G. ruber* shells (10–20 specimens) were picked from the above coarse fractions, ultrasonically cleaned and then tested using the stable isotope mass spectrometer. The $\delta^{18}O$ results are reported versus PDB after calibration with NBS 19 (Table S5). The average test accuracy is ± 0.07‰.

AMS ^{14}C dating of planktonic foraminiferal shell and woody debris was measured at Beta Analytic Laboratory (USA). The selection principle of test materials was to preferentially select clean and intact shells of *G. ruber*. If their weights were less than the minimum requirement for testing (~6 mg), the planktonic foraminifera of other genera were also picked for supplementation. After inspection, it turned out that three samples (Md01, Md02, and Md03) contain abundant *G. ruber*, and three samples (Md04, Md06, and Md07) require mixed species of planktonic foraminifera. Specifically, Md04 and Md06 samples consist of *G. ruber* and *Globigerinoides sacculifer*, and Md07 sample consists of *G. ruber*, *Globigerinoides sacculifer*, *Globorotalia menardii*, *Globigerina bulloides*, *Globigerinella siphonifera*, *Pulleniatina obliquioculata*, and *Neogloboquadrina dutertri*. For the other four samples (Md05, Md08, Md09, and Md10) with insufficient foraminiferal shells, fresh and large woody debris was used for dating instead (Table 1).

Spectral analysis was mainly performed following the user manual of the Acycle software (Li et al., 2019). Taking the Si/K ratio as an example, the elemental ratio data were first sorted to remove blank values. Then, the data were interpolated into equally spaced data. Linear interpolation was performed using the MatLab's *interp1* function (Li et al., 2019). The default sampling rate for interpolation is the median sampling rate (0.5 yr/mm) of the data. The interpolated data were then detrended using the Lowess method with 400 window lengths. Finally, the processed data were analyzed using multi-taper, Blackman-Tukey, and maximum-entropy methods. For the multi-taper method, the data were analyzed with the 2π time bandwidth, classic AR red noise (no smoothing), and no zero-padding. For the Blackman-Tukey method, the data were analyzed with the classic AR red noise (no smoothing) and without zero-padding. For the maximum-entropy method, the data (~12,000 points) were estimated with an autoregressive order (order=2,000) and

5,000 discrete Fourier transforms. The first two methods were performed in the Acycle software, and the last one was performed in the MatLab software. The spectral analysis of the Zr/K ratio and grayness followed the same procedure. The original results and parameter settings of all spectral methods are given in Tables S6–S12.

3. Chronology

Seven AMS ^{14}C dating and three oxygen isotope stratigraphic ages are accepted as age control points to establish an age model of Core MD05-2892. Ten radiocarbon dates were corrected from raw results into calendar ages (Table 1) using the CALIB software (version 8.0; Stuiver and Reimer, 1993) with the Intcal20 curve (Reimer et al., 2020) for woody debris dates and the Marine20 curve (Heaton et al., 2020) for planktonic foraminifera dates without a further adjustment for a regional radiocarbon reservoir age. Calendar ages at 0.05, 1.01, 2.38, 5.82, 9.65, 13.25, and 13.72 m gradually increase from 2.21 to 22.00 cal ka BP, indicating that the sedimentary sequence is normally and continuously deposited. As a result, these seven ages are accepted. However, calendar ages at 3.60 m, 3.64 m, and 9.49 m appear anomalous and are attributed either to secondary diagenesis or to remobilization of pre-existing materials (Supplementary Data Figs. S1 and S2), therefore they are not accepted. In addition, $\delta^{18}O$ and Ca data of Cores MD05-2892 and MD05-2893 are highly consistent in terms of value ranges (–1 to –3.7‰ for $\delta^{18}O$ data; 1,300–39,000 cps for Ca data) and glacial-interglacial variations (Fig. 2). Specifically, $\delta^{18}O$ values are lower and Ca values are higher in the Holocene than those in the last glaciation. Compared with the oxygen stratigraphy of Core MD05-2893 (Jiwarungrueangkul et al., 2019), three oxygen stratigraphic ages (10.17, 13.06, and 14.31 cal ka BP) are identified for Core MD05-2892 (Fig. 2). These oxygen stratigraphic ages

show a great agreement with the seven accepted AMS ^{14}C ages in terms of the depth-age relationship, therefore these ages are accepted as age control points.

Table 1. AMS ^{14}C dating and oxygen isotope stratigraphic ages of Core MD05-2892

Sample ID	Depth (m)	Sample material	AMS ^{14}C age (yr BP)	Calendar age (cal yr BP, 1σ)
Md01	0.05	*G. ruber*	2,670 ± 30	2,208 (2,130–2,286)
Md02	1.01	*G. ruber*	4,700 ± 30	4,748 (4,667–4,829)
O1	2.09	–	–	10,170 [a]
Md03	2.38	*G. ruber*	9,490 ± 40	10,175 (10,097–10,252)
O2	3.01	–	–	13,060 [a]
O3	3.60	–	–	14,312 [a]
Md04	3.60	Mixed foraminifers	9,670 ± 30	10,394 [b] (10,302–10,485)
Md05	3.64	Woody debris	14,920 ± 40	18,229 [b] (18,203–18,255)
Md06	5.82	Mixed foraminifers	13,170 ± 40	15,004 (14,897–15,111)
Md07	9.49	Mixed foraminifers	5,240 ± 30	5,397 [b] (5,320–5,474)
Md08	9.65	Woody debris	15,040 ± 40	18,269 (18,242–18,296)
Md09	13.25	Woody debris	15,940 ± 40	19,234 (19,149–19,318)
Md10	13.72	Woody debris	18,050 ± 70	22,002 (21,910–22,094)

[a] Obtained by comparing the oxygen isotope stratigraphy and XRF core scanning Ca value of Core MD05-2892 with those of Core MD05-2893.

[b] Not accepted in the final age model.

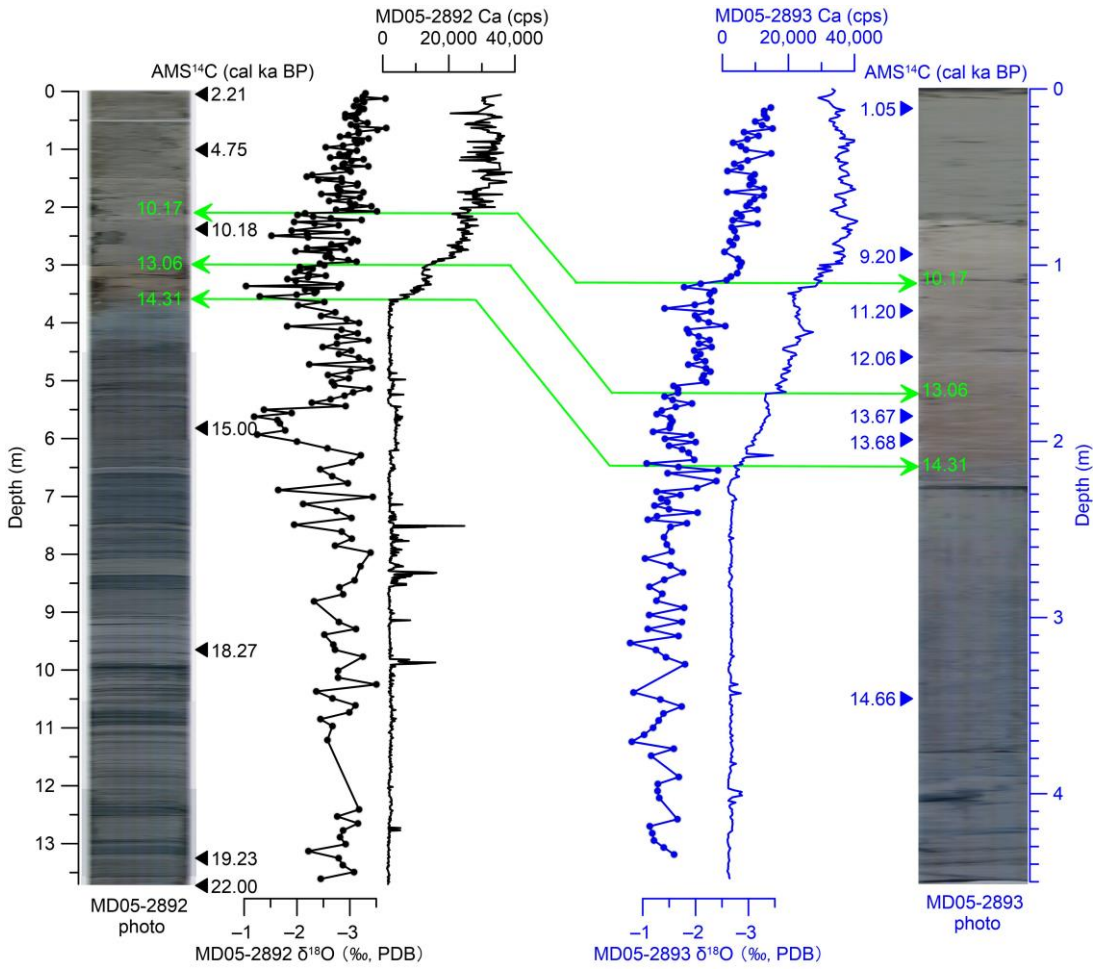

Fig. 2. Correlation of $\delta^{18}O$ obtained on *G. ruber* and Ca data of Core MD05-2892 with those of Core MD05-2893. Photos of the two cores are also displayed (Laj et al., 2005). The unaveraged Ca results of Cores MD05-2892 and MD05-2893 (unpublished) are from XRF core scanning elements at 1 cm resolution with the same parameter settings. AMS ^{14}C ages and $\delta^{18}O$ results of Core MD05-2893 are from Jiwarungrueangkul et al. (2019). The AMS ^{14}C ages of Core MD05-2893 were re-calibrated using the Marine20 curve (Heaton et al., 2020) without a further adjustment, and the age model of this core was constructed using the Clam package with the smooth spline (Blaauw, 2010). The oxygen isotope stratigraphic ages are indicated (green).

The ten age control points were processed with the Clam package (Blaauw, 2010) using a smooth spline type to obtain the final age model of Core MD05-2892 (Fig. 3). The model shows that the age of the sediments from 0 to 3.6 m rapidly increases from 2.0 to 14.3 cal ka BP. During this period, the error range of the model is 0.03–0.80 ka with an average error of 0.29 ka. The age of sediments from 3.6 to 13.7 m slowly increases from 14.3 to

20.8 cal ka BP. The error range for this interval is 0.05–2.00 ka with a mean error of 0.91 ka. The error range (the 95% confidence interval) of this age model is calculated in the Clam package using the Mote Carlo approach with 1,000 times iterations (Blaauw, 2010). Within the error range, the Clam calculates the weighed mean of all calendar ages for every depth to find the single best depth-age result (Blaauw, 2010). In addition, previous study has used the best age-depth result from a Clam age model for the paleo-environment interpretation in the southern South China Sea (Huang et al., 2019). Therefore, the best age-depth result is the optimal result from the Clam age model, and is used for further analysis. The best age-depth result shows that Core MD05-2892 provides a continuous sedimentation sequence spanning the time interval from 2.0 to 20.8 cal ka BP. Furthermore, 1-mm resolution XRF core scanning data have a sample resolution of 0.6 yr/mm (0.4–1.8 yr/mm) on average in 3.6–13.7 m.

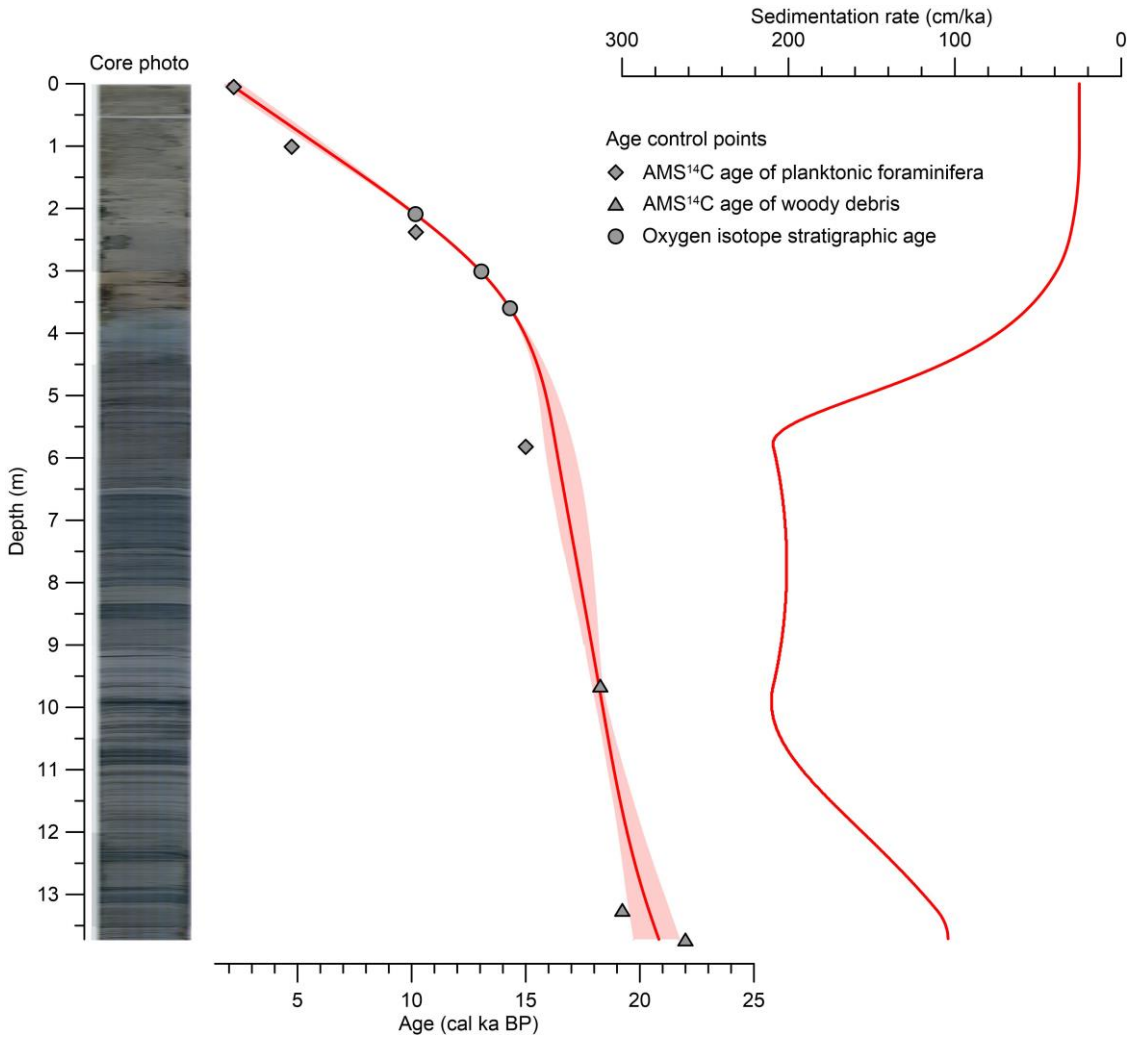

Fig. 3. Age model of Core MD05-2892 constructed by the Clam package based on accepted 10 age control points (Table 1). The thicker line presents the best modelling result and the shadow indicates the level of 95% confidence (Blaauw, 2010). Core photo and sedimentation rate are also displayed.

The sedimentation rate of Core MD05-2892 shows a gradual increase from 25 to 33 cm/ka during 0–12.0 cal ka BP, a sharp increase from 33 to 209 cm/ka during 12.0–16.3 cal ka BP, a relatively stable pattern (~206 cm/ka) during 16.3–18.4 cal ka BP, and an overall decrease from 210 to 104 cm/ka during 18.4–20.8 cal ka BP. The average sedimentation rate is about 6 times higher in the last glaciation (~161 cm/ka) than that in the Holocene (~27 cm/ka), which is similar to the variations (19–675 cm/ka in the last glaciation and 6–57 cm/ka in the Holocene) recorded by previous studies in the Sunda Slope (Pelejero et

al., 1999; Steinke et al., 2003, 2008; Huang et al., 2016, 2019; Jiwarungrueangkul et al., 2019; Jiwarungrueangkul and Liu, 2021). This corroborates the reliability of our age model.

4. Results

4.1. Dark layers and grayness

Dark layers are defined by grayness data and photo manual statistics. Due to high-resolution variabilities of the grayness data, we use the 200-point average data of the grayness data to show the general variation of the grayness (Fig. 4). If the 3-point average of grayness is lower than the 200-point average of grayness at a depth, and the sediment at that depth is laminar, then the laminar sediment at that depth is defined as a dark layer. Based on this principle, we identified 739 dark layers with thickness ranges from 1 to 32 mm in 3.6–13.7 m. Among these dark layers, 34 dark layers are thicker than 10 mm, and 484 dark layers have a thickness of ~4 mm. There is no clear regularity in depth or time variations of the dark-layer thickness (Figs. 4 and S3). Interestingly, the dark layers in 3.6–4.1 and 5.5–6.1 m are unobvious by manual statistics of the core photos (Fig. 4). Relatively, the other intervals are defined as dark-layer enriched intervals.

The grayness value of Core MD05-2892 ranges from 24 to 126 with glacial-interglacial variations (Fig. 4). The grayness value is lower in the last glaciation (average 85) than that in the Holocene (average 102). During the last glacial period, the main sedimentary feature of the core is the laminated sequence (Fig. 4). In the glacial laminated sequence, grayness value shows highly fluctuating low values (ranging in 24–115) in dark-layer enriched intervals and relatively stable high values (average 91) in other intervals (i.e., 3.6–4.1 and 5.5–6.1 m) (Fig. 4). In the light and dark layers within laminae, grayness

value shows opposite trends upwards (Fig. 5). The grayness value decreases and then increases in the dark layer, while it increases and then decreases in the light layer (Fig. 5).

4.2. XRF core-scanning elements

XRF core-scanning elements of Core MD05-2892 show large changes for six elements, including Ca, Zr, Si, K, Fe, and Ti (Fig. 4). The total intensity (sum of the six element intensities) is not a constant value, but shows a glacial-interglacial variation. This variation may be related to changes in chemical concentrations and physical properties of Core MD05-2892. The value and variation of the total intensity are similar to those of the Fe element intensity, possibly due to the high atomic weight and content of Fe resulting in high intensity values and apparent variations. Without constant-sum constraints, each element shows the independent variations, and element intensity variations could indicate changes in the element content of the core. The contents of the six elements show clear glacial-interglacial variations. In general, Zr, Si, K, Fe, and Ti show alike variation patterns, while variation of Ca is inversely correlated to the other five elements. The content of Ca is higher in the Holocene than that in the last glaciation, while the contents of the other five elements in the last glaciation are higher than those in the Holocene (Fig. 4).

On a short-time scale, the contents of the six elements show two distribution patterns in the glacial laminated sequence (Figs. 4 and 5). The content variations of Ca, Zr, and Si are generally similar, and they are opposite to those of K, Fe, and Ti. The contents of Ca, Zr, and Si display high values with high amplitude fluctuations in dark-layer enriched intervals and relatively stable low values in the other intervals, whereas the variations of the other three elements basically mirror with those of Ca, Zr, and Si (Fig. 4).

Furthermore, Ca, Zr, and Si values show an increasing upwards and then decreasing trend in dark layers, and the opposite trend is observed in light layers (Fig. 5). K, Fe, and Ti values decrease upwards at first and then increase in dark layers and show the opposite trend in light layers. Moreover, compared with the 200-point averages of elements in dark layers, the values of Ca, Zr, and Si are generally higher, and the values of K, Fe, and Ti are generally lower (Fig. 5). Such features are impossible to be interpreted as the results of the terrigenous input dilution.

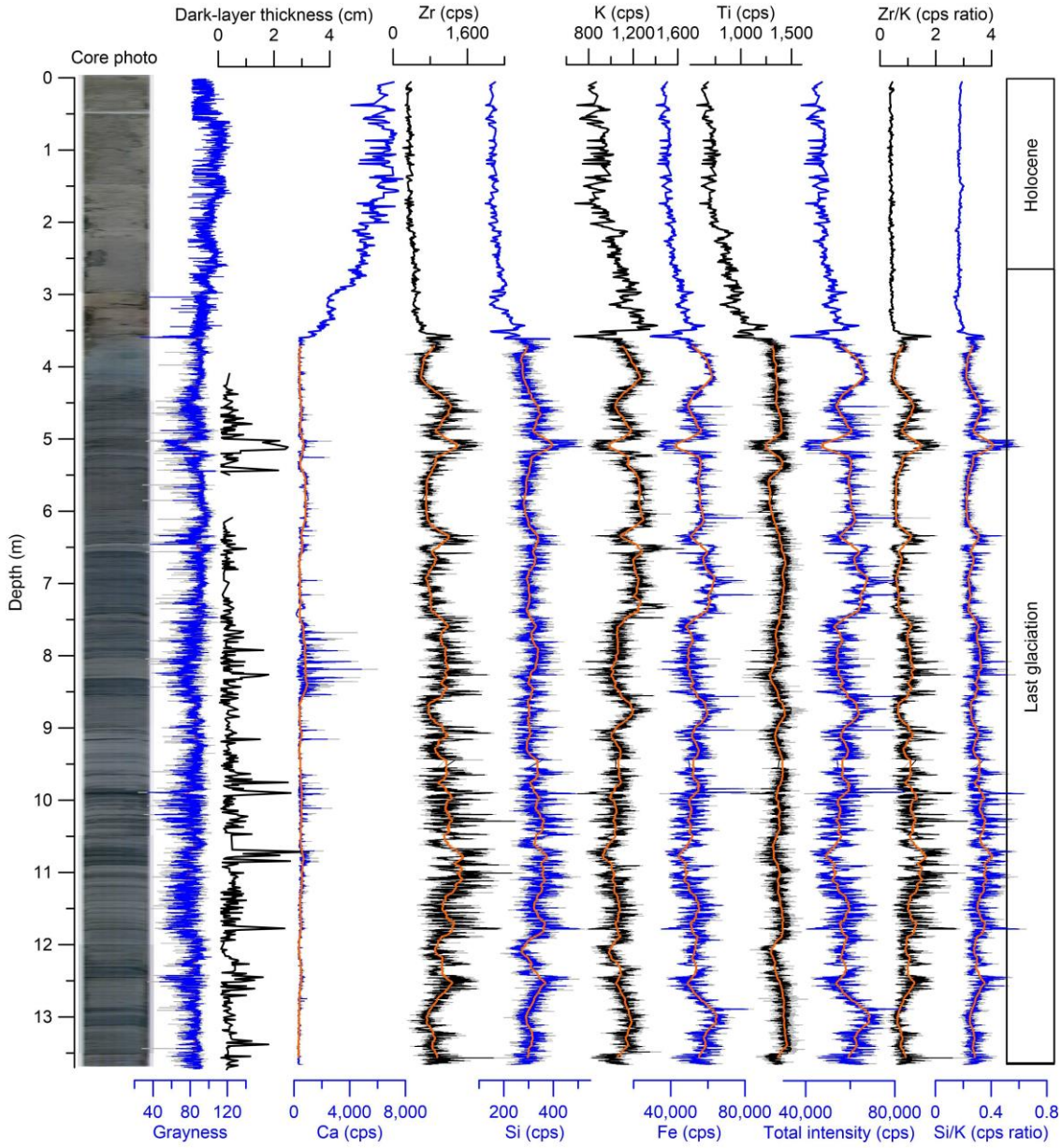

Fig. 4. Depth-scaled downcore variations of six elements in Core MD05-2892. Core photo, dark-layer thickness, grayness, total intensity (sum of the six element intensities), elemental ratios, and age framework are also displayed. Gray, blue or black, and orange lines of elements and grayness in the last glaciation are original, 3-point average, and 200-point average data, respectively.

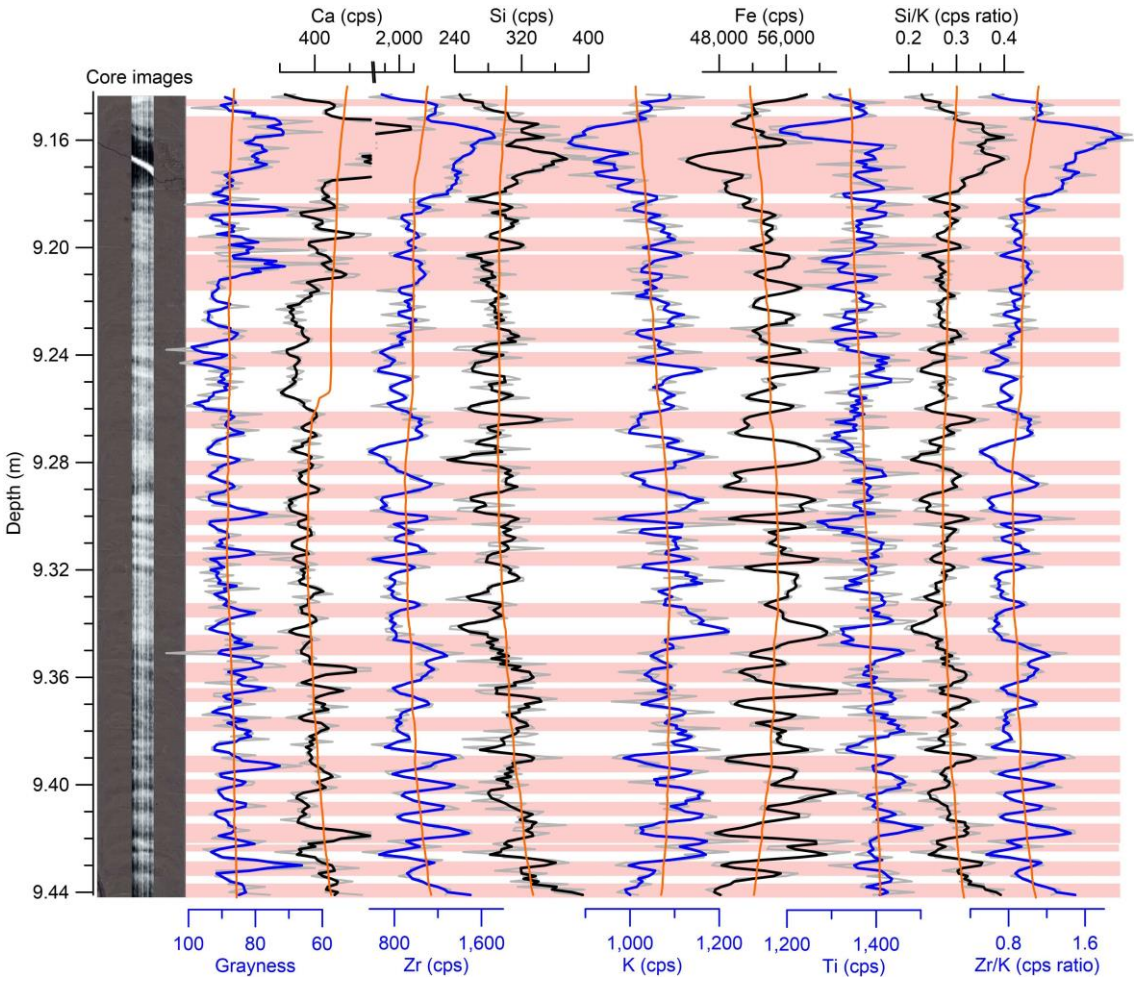

Fig. 5. Depth-scaled downcore profiles of six elements in the 9.1–9.4 m interval of Core MD05-2892. Core images (optical photo and X-ray image), grayness, and elemental ratios are also indicated. Gray, blue or black, and orange lines are original, 3-point average, and 200-point average data, respectively. The x-axis of Ca element is broken from 560 cps to 1,200 cps in 9.15–9.18 m. Pink bars indicate dark layers.

4.3. Coarse fractions

The coarse fractions of Core MD05-2892 since 20.8 cal ka BP have contained wood (0.2–10.0 mm, average 0.6 mm), biotite (0.1–0.5 mm, average 0.2 mm), quartz (0.07–0.1 mm,

average 0.1 mm), clayey nodule (0.1–1.0 mm, average 0.2 mm), amber (0.05–0.5 mm, average 0.2 mm), bivalve shell (1.5–4.0 mm, average 1.2 mm), and foraminifera (0.08–0.1 mm, average 0.09 mm).

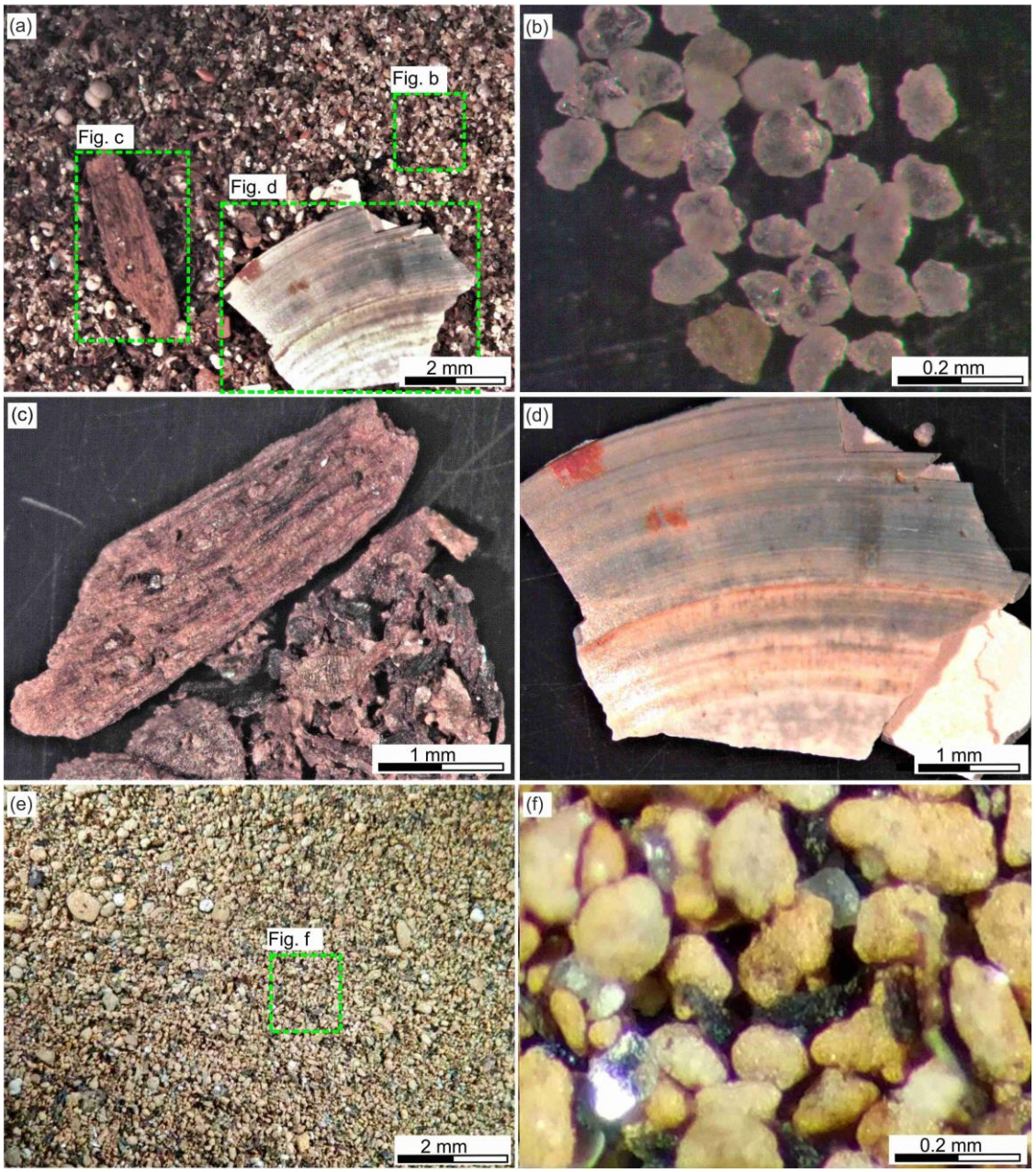

Fig. 6. Coarse-fraction microscopic observation on typical laminae of Core MD05-2892. (a) Coarse fractions in a typical dark layer (3.59–3.61 m). (b) Quartz. (c) Woody debris. (d) Bivalve shell. (e) Coarse fractions in a typical light layer (8.68–8.70 m). (f) Reddish-brown clayey nodule. Dashed green rectangles indicate zoom-out views.

The temporal distribution of these coarse fractions shows distinct differences between the last glaciation and the Holocene intervals. During the last glaciation, the coarse fractions are composed mainly of terrigenous clastics, including wood, biotite, quartz, clayey nodule, and amber, while during the Holocene the coarse fractions are dominated by planktonic foraminifera. Although coarse-fraction compositions are similar in the last glaciation, the abundance of coarse fractions is much higher in dark-layer enriched intervals than that in the other intervals. Furthermore, the coarse fractions are different between dark and light layers. The coarse fractions of dark layers are in higher abundances and rich in woody debris, bivalve shell, and quartz grain, whereas those of light layers are in less abundances and rich in reddish-brown clayey nodule (Fig. 6).

5. Discussions

5.1. Provenance of terrigenous sediments

The provenance of terrigenous sediments of Cores MD05-2892 and MD05-2893 should be similar because of almost same locations of the two cores (Fig. 1). Clay mineral and major element results of Core MD05-2893 have indicated that the variability of the terrigenous sediment input since the last glaciation has been mainly driven by sea-level changes (Jiwarungrueangkul et al., 2019). During the last glacial sea-level lowstand, terrigenous sediments were mainly supplied from the western Sunda Shelf including the Chao Phraya-Johore River and the North Sunda River systems (Fig. 1). During the sea-level rise and highstand of the Holocene, these two paleo-river systems were flooded, resulting in a limited terrigenous contribution from the western Sunda Shelf. These findings are supported by previous studies in the Sunda Slope (Steinke et al., 2003, 2008; Huang et al., 2016). Therefore, the terrigenous sediment provenance of Core MD05-2892 during the last glacial sea-level lowstand should be the western Sunda Shelf.

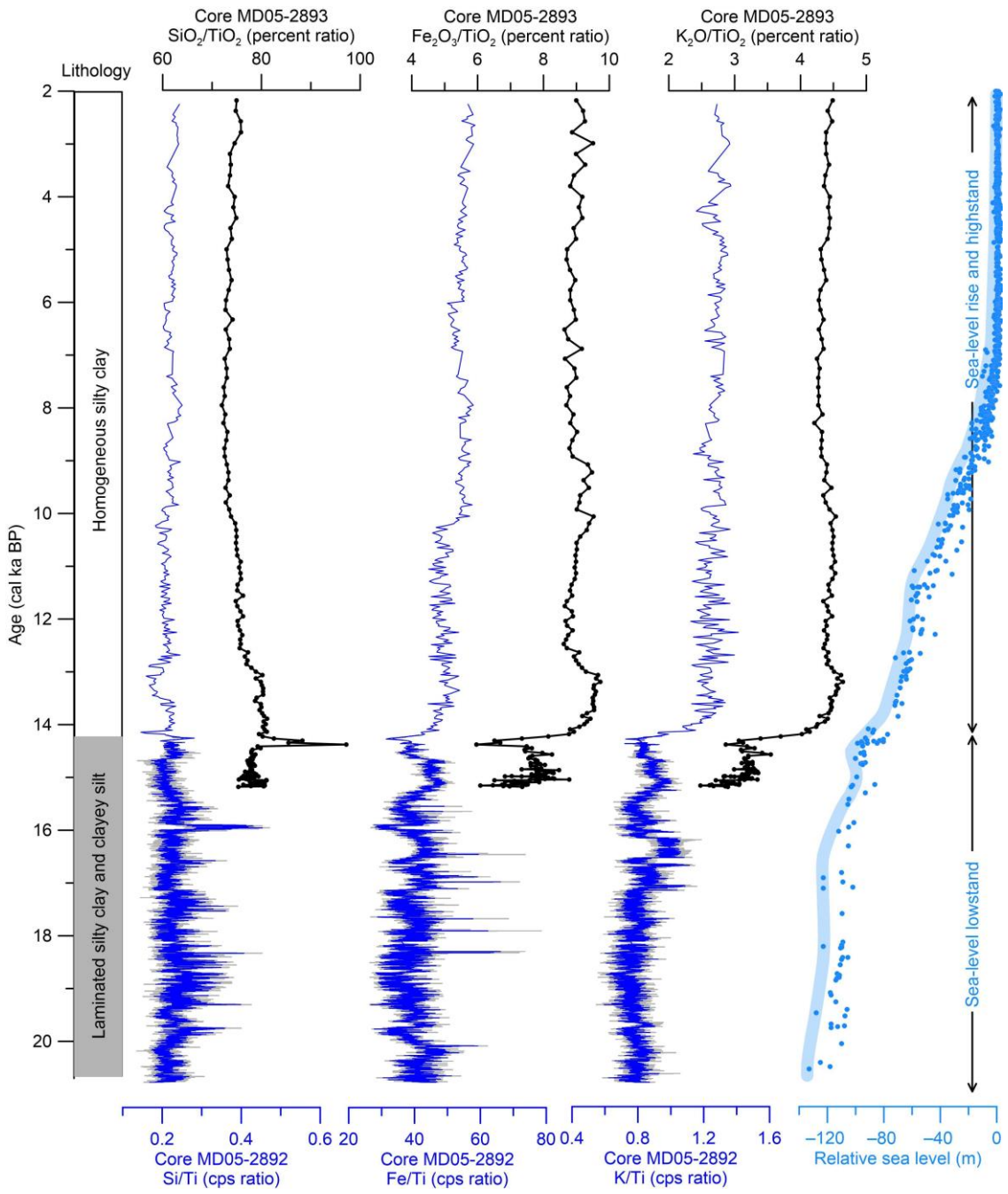

Fig. 7. Major element ratios of Cores MD05-2892 and MD05-2893. Lithology of Core MD05-2892 and relative sea level data (Lambeck et al., 2014) are also indicated. Gray and blue lines of the ratios in the last glaciation are original and 3-point average data, respectively.

Variation patterns of major element ratios between Cores MD05-2892 and MD05-2893 were compared to confirm the same sediment provenance of these two cores. As a terrigenous element with refractory nature, Ti has been widely used as a standardization to

eliminate interfering signals (Xie et al., 2014; Gebregiorgis et al., 2020). Temporal variations of Si/Ti, Fe/Ti, and K/Ti ratios of Core MD05-2892 and SiO_2/TiO_2, Fe_2O_3/TiO_2, and K_2O/TiO_2 ratios of Core MD05-2893 are well correlated to sea-level changes (Fig. 7). Variation patterns of the Si/Ti and SiO_2/TiO_2 ratios are similar, and they are opposite to those of the Fe/Ti, Fe_2O_3/TiO_2, K/Ti, and K_2O/TiO_2 ratios. The Si/Ti and SiO_2/TiO_2 ratios show high values with high amplitude fluctuations during the last glacial sea-level lowstand and low values during the sea level rise and highstand. On the contrary, the Fe/Ti, Fe_2O_3/TiO_2, K/Ti, and K_2O/TiO_2 ratios show highly fluctuating low values during the last glacial sea-level lowstand and high values during the sea level rise and highstand. Such similar patterns of major element ratios of these two cores indicate the same geochemical characteristics, confirming that the terrigenous sediment provenance of these two cores has been the same since the last glaciation.

The most prominent feature of Core MD05-2892 during the last glacial sea-level lowstand is laminar sediments (Fig. 7). Compared with the light-layer sediments, the dark-layer sediments have a relatively higher abundance of coarse fractions and are relatively rich in woody debris, bivalve shell, and highly matured quartz (Fig. 6). These clastics accumulate usually near the coastal zone (Allen, 1981; Leithold and Hope, 1999). Therefore, dark- and light-layer sediments represent increased and reduced supplies of coastal coarse sediments in the western Sunda Shelf during the last glacial sea-level lowstand, respectively.

5.2. Periodicity of lamina occurrences

Grayness and element compositions are different between dark and light layers in the laminated sequence of Core MD05-2892. Dark layers are characterized by higher values

of Zr and Si as well as lower values of K and grayness than their 200-point averages, whereas light layers are characterized by the opposite (Fig. 5). The Si and Zr are mainly enriched in coarse-grained sediments such as quartz and zircon, and K is mainly found in fine-grained sediments such as clay minerals (Fig. 6). Therefore, grayness, Si/K ratio, and Zr/K ratio can be used as proxies of lamina occurrences, e.g., lower grayness values and higher elemental ratios than their 200-point averages representing dark layers (Fig. 5). Moreover, higher elemental ratios in dark-layer sediments than in light-layer sediments indicate coarser grain sizes.

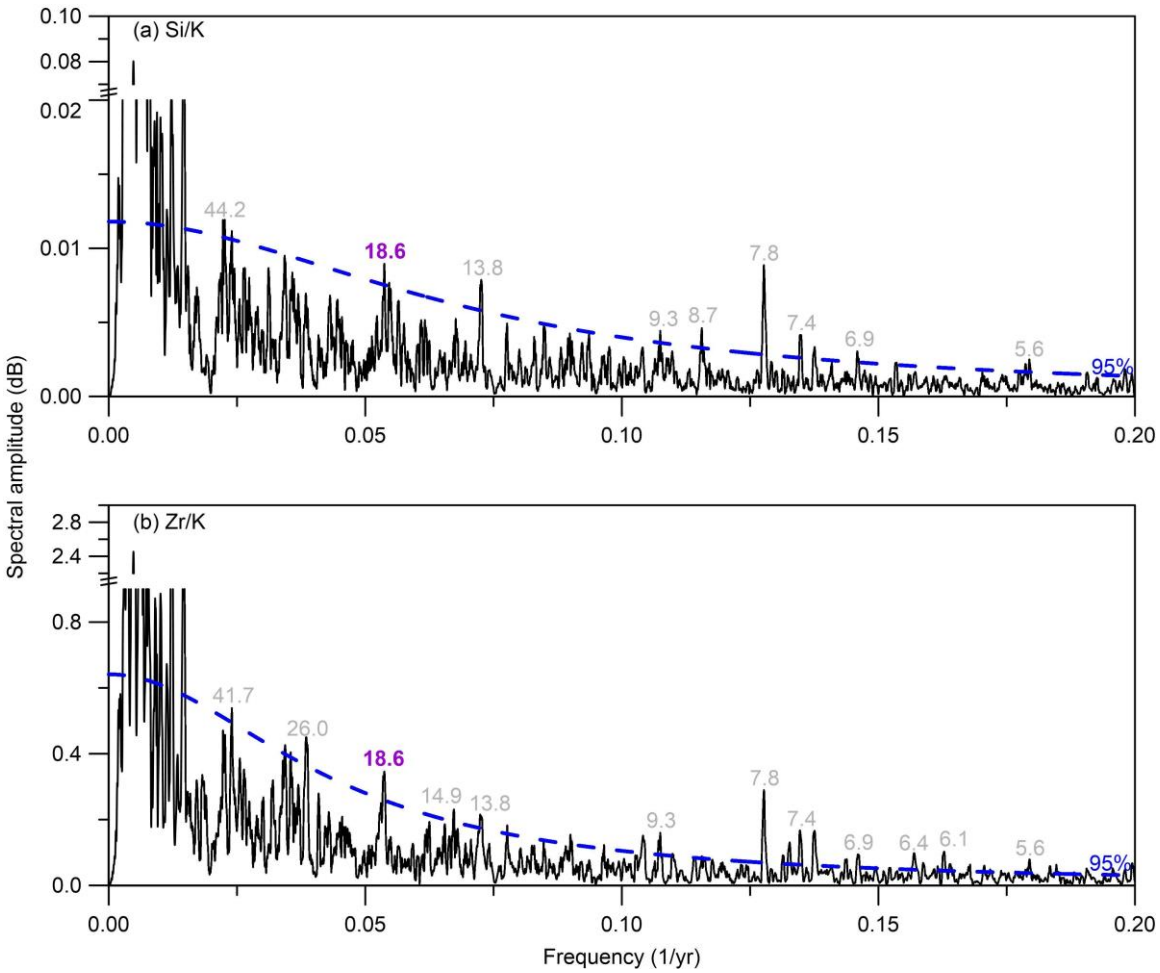

Fig. 8. Multi-taper spectral analyses of (a) Si/K ratio and (b) Zr/K ratio of Core MD05-2892 during the last glacial 14.3–20.8 cal ka BP. Blue dashed lines are the 95% confidence level. The y-axis of Si/K and Zr/K ratios is broken at 0.02–0.07 and 0.9–2.2, respectively.

Multi-taper method spectral analyses of grayness, Si/K ratio, and Zr/K ratio of Core MD05-2892 during the last glacial 14.3–20.8 cal ka BP were performed using the Acycle software (Li et al., 2019) to characterize periods of lamina occurrences. Considering the sample resolution (<1.8 yr/mm) of 1-mm resolution XRF core scanning data and the temporal interval of adjacent dark layers (average=7 yr, maximum<50 yr; Fig. S3), we mainly identify the 5–50-yr period from the spectral results. The spectral results of the Si/K ratio reveal peaks centered at 5.6, 6.9, 7.4, 7.8, 8.7, 9.3, 13.8, 18.6, and 44.2 yr above the 95% confidence limit (Fig. 8a). The spectral results of the Zr/K ratio reveal peaks near 5.6–7.8, 9.3, 13.8, 14.9, 18.6, 26.0, and 41.7 yr (Fig. 8b). The spectral result of grayness data contains many peaks including the 18.6 yr (Fig. S4). Such many peaks in the grayness may be related to interfering signals in grayness extraction processes. When optical signals were extracted from core photos, the extracted the dark signals contained not only dark-layer signals but also other interfering signals (black dots caused by low-resolution photos, black non-laminated sediments, etc.). Considering the low quality of the grayness spectral result, this result was not analyzed furthermore.

Among these spectral peaks, the 18.6 yr peak recorded by the laminae is not only the first observation in the deep South China Sea, but also a very rare feature for tropical deep-sea laminae (Ojala et al., 2012). To confirm the reliability of this peak, we have evaluated the influence of the uncertainty in our age model (Fig. 3) on the spectral results. Using the Si/K ratio as an example, the Si/K ratio was interpolated into equally spaced data, and then the data were detrended. The processed ratio data were analyzed using the multi-taper spectral method in different age results (minimum and maximum age results in the smoothed Clam age model, Fig. 3). The spectral results above the 95% confidence level show the 19.7-yr peak in the minimum age and the 20.6-yr peak in the maximum age (Fig.

9). In addition, the multi-taper spectral result of the Si/K ratio in the linearly-connected age model shows the 19.0-yr peak above the 95% confidence level. This spectral result is not shown because we chose to use the smoothed Clam age model instead of the interpolated model. These spectral peaks could be the surrogates for the 18.6-yr peak. Therefore, although different age results would cause a slight shift of the 18.6-yr peak with a maximum error of 2.0 yr, the ~18.6-yr peak is a reliable existence.

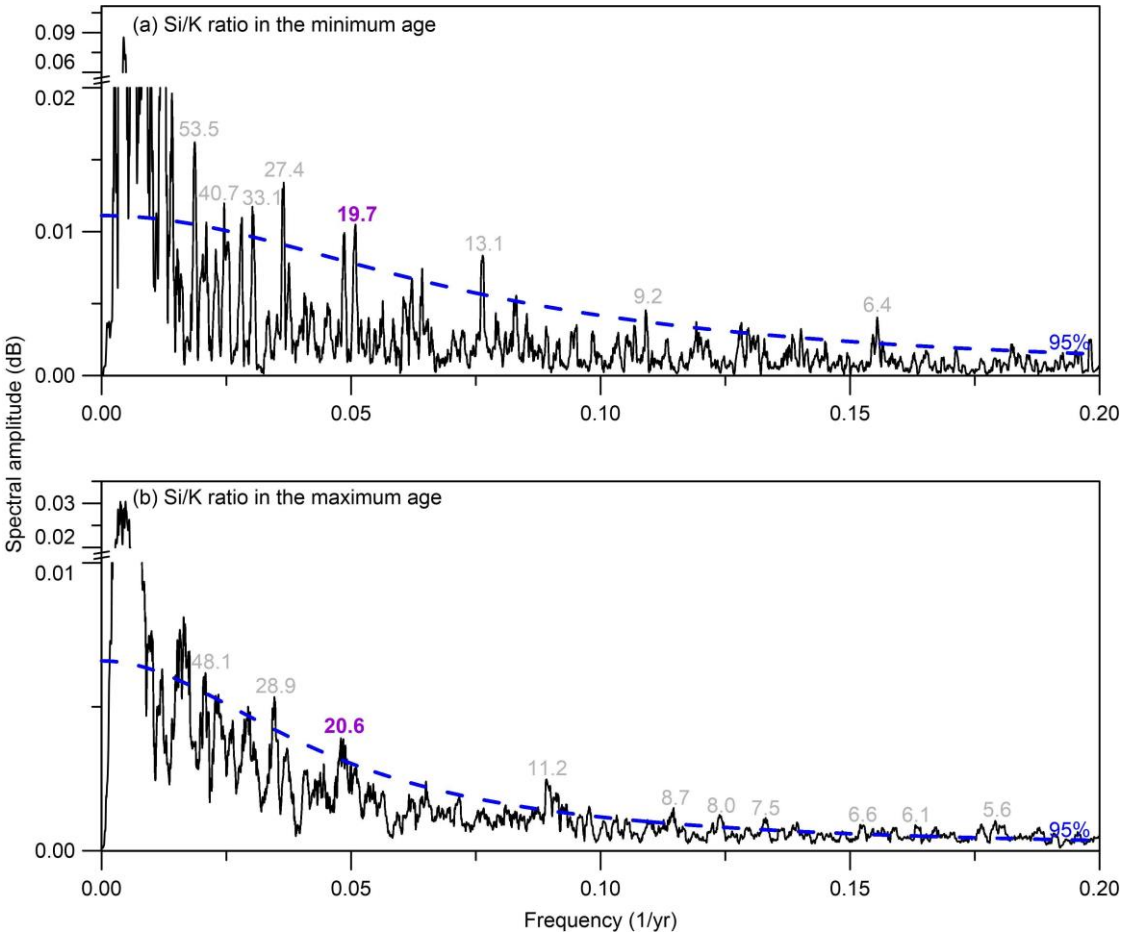

Fig. 9. Multi-taper spectral analyses of the Si/K ratio in the (a) minimum-age and (b) maximum-age results for the glacial laminated sequence in Core MD05-2892. Blue dashed lines are the 95% confidence level. The y-axis of Si/K ratio in the minimum and maximum ages is broken at 0.02–0.06 and at 0.01–0.02, respectively.

Additionally, several independent spectral methods (multi-taper, maximum entropy, and Blackman-Tukey) were highly recommended to be applied before drawing conclusions

about the spectrum, because these spectral methods are complementary (Ghil et al., 2002). Accordingly, maximum-entropy and Blackman-Tukey spectral analyses of the processed Si/K ratio in the best Clam age (Fig. 3) were performed to corroborate the reliability of the 18.6-yr period obtained by the multi-taper spectral method. Spectral results of these two methods both show the 18.7-yr peak (Fig. 10). This spectral peak could be the surrogate for the 18.6-yr peak. Therefore, the analyses of different spectral methods in the same age result and the same spectral method in different age results all confirm the reliable existence of the ~18.6 yr peak.

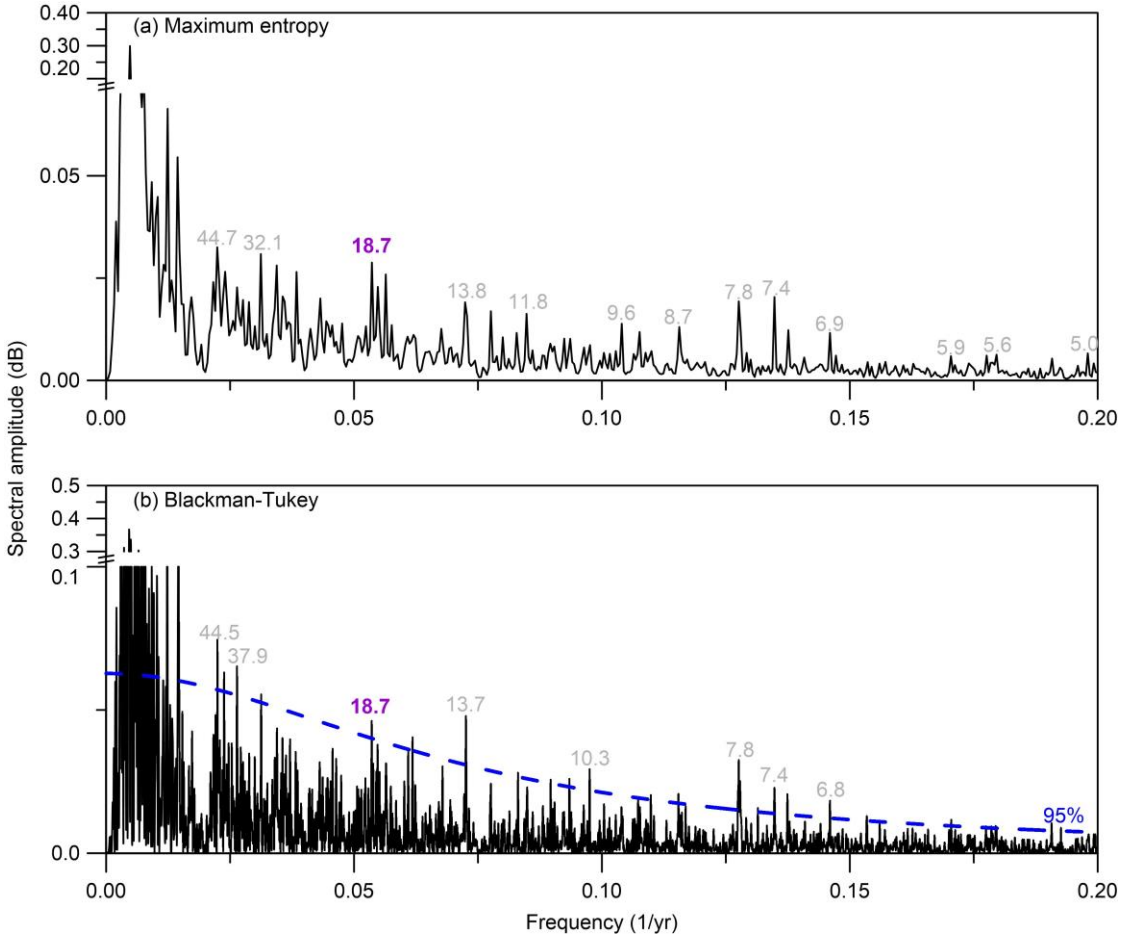

Fig. 10. (a) Maximum entropy and (b) Blackman-Tukey spectral analyses of the Si/K ratio at Core MD05-2892 during the last glacial 14.3–20.8 cal ka BP. Blue dashed line is the 95% confidence level. The y-axis of the maximum entropy and Blackman-Tukey methods is broken at 0.07–0.2 and 0.1–0.3, respectively.

Although long-term ENSO or solar variabilities could explain the ~18.6-yr peak, this peak is best interpreted as the lunar nodal tidal cycle. Long-term ENSO and solar variabilities both could influence the compositional characteristics of sediments by regulating regional precipitation (e.g., Kiefer and Karamperidou., 2019; Shi et al., 2021). For example, the possible formation mechanism of laminae in the Bohai Bay Basin is related to fluvial input variations triggered by solar-radiation-driven precipitation (Shi et al., 2021). Accordingly, dark layers within the laminae are characterized by lower values of Ca and higher values of Si and Ti compared with light layers (Shi et al., 2021). However, dark layers within laminae of Core MD05-2892 are characterized by lower values of Ti and higher values of Ca and Si compared with light layers (Figs. 4 and 5). This feature is unlikely to be interpreted as the increased input of terrigenous clastics due to the enhanced rainfall, but it could be explained as the increased input of coastal coarse sediments due to the enhanced hydrodynamic sorting. This explanation is also supported by other core sediments in the East China Sea (Tian et al., 2019). For example, coarse-grained sediments of Cores C0702 and DH6-1 are relatively rich in Ca and Si and depleted in Ti, which are interpreted as the remobilization of coastal coarse sediments triggered by the strong hydrodynamic sorting (Tian et al., 2019). Among hydrodynamic sorting cycles in our knowledge, the ~18.6-yr period is most likely the lunar nodal tidal cycle. This interpretation is consistent with the ~18.6-yr cycle explanation of laminar sediments in the Santa Barbara Basin and the Cariaco Basin (Berger et al., 2004; Black et al., 2009). In addition, other non-18.6 yr peaks may be related to different sedimentary dynamics and are not explored too much here.

To confirm the aforementioned interpretation of the ~18.6 yr cycle in the lamina occurrences of Core MD05-2892, it would be best to perform a correlation analysis

between the elemental ratio (e.g., Si/K ratio) and the lunar nodal tidal record. However, we could not obtain the real lunar nodal tidal record (the reference data for the correlation analysis) in the last glaciation. To solve this problem, a cosine curve with the 18.6-yr period was constructed as the reference data (Table S13). Using the MatLab software package of Grinsted et al. (2004) for the wavelet-coherence analysis, the wavelet coherence between the processed Si/K ratio and the calculated lunar nodal tidal record shows a significant correlation between these two data at the ~18.6-yr period during the last glacial 14.3–20.8 cal ka BP (Fig. 11). This suggests that the ~18.6-yr cycle of the lamina occurrences could be reasonably interpreted as the lunar nodal tidal cycle.

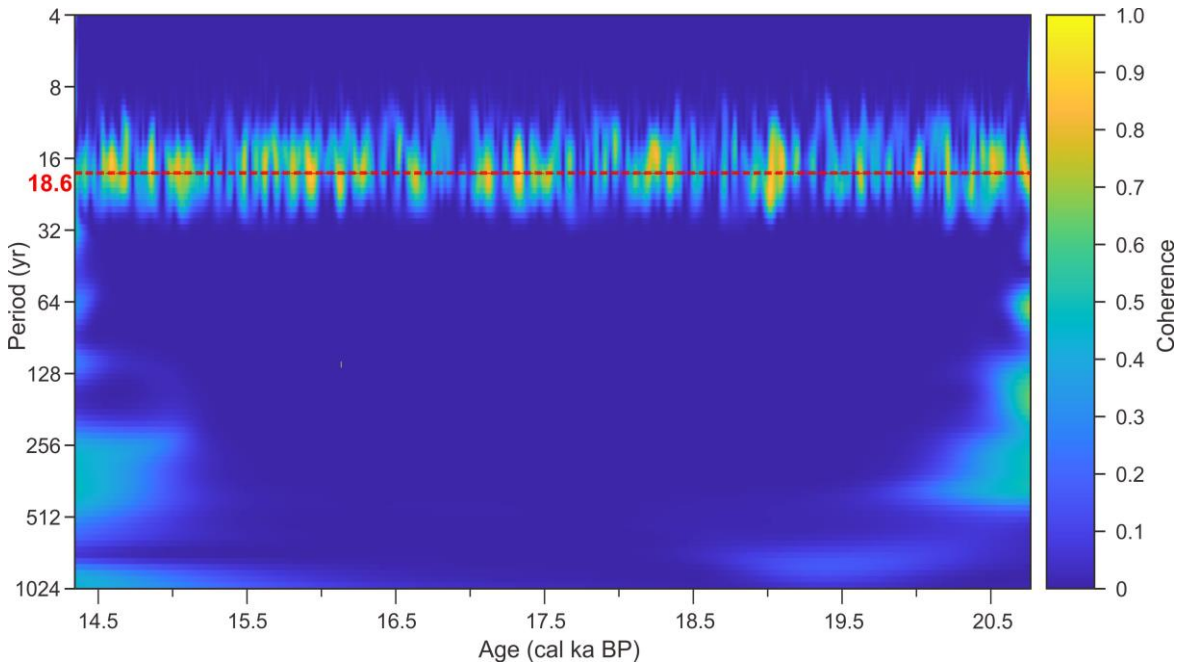

Fig. 11. Wavelet coherence between the Si/K ratio of Core MD05-2892 and the calculated lunar nodal tidal record during the last glacial 14.3–20.8 cal ka BP. Red dashed line represents the 18.6 yr.

5.3 Cross-slope transport of laminar sediments

Occurrence periodicity and sedimentary feature of one laminar couplet in Core MD05-2892 indicate that the transport of coastal coarse sediments from the western Sunda Shelf

to the deep sea was influenced by tidal intensity variations in one lunar nodal tidal cycle (Fig. 12). Tidal intensity variation was reflected as position changes in mean high water lines, and it was controlled by periodically variational positions of the Moon, the Earth, and the Sun in one tidal cycle (Pugh, 1987; Oost et al, 1993). For example, tidal intensity gradually strengthened and then weakened as the Moon-Earth-Sun positions were gradually aligned and in quadrature. When the tidal intensity was higher than a certain threshold (Fig. S5), the coastal coarse sediments began to be remobilized and mixed with the surrounding seawater to form a high-density flow with suspended load. Such hyperpycnal flow could transport the coastal coarse sediments to the deep sea to form dark layers. Further, the coastal sediments transported via the hyperpycnal flow became gradually coarser and then finer when the tidal intensity strengthened at first and then weakened. In this process, when the ascending node coincided with the spring equinox, the resultant force of the Moon and the Sun on the Earth was the largest due to the co-linearity of the Moon-Earth-Sun positions (Kaye and Stuckey, 1973; de Boer and Alexandre, 2012; Fig. 12a). Accordingly, mean high water line was at the highest position and tide-eroded capacity increased by 10–20% (Oost et al., 1993; Gratiot et al., 2008; Peng et al., 2019; Fig. 12a). Under the influence of this maximal tidal intensity, large amounts of the coarse sediments were transported to the deep sea via the hyperpycnal flow (Fig. 12a). When the tidal intensity was lower than the threshold, weakened ocean current was insufficient to remobilize the coarse sediments, but it could transport fine-grained sediments to the deep sea via the hemipelagic dispersal to form the light layers (Fig. 12b). When the Moon-Earth-Sun positions were gradually aligned again, the light layer gradually disappeared, while the dark layer gradually occurred again. In fact, sedimentary features of dark layers, with sand-containing clayey silt dominated, plant debris enriched, coarsening and then fining upwards, and gradual bottom contacted, are inconsistent with

gravity-flow characteristics (Shanmugam, 2020), but they are consistent with sedimentary characteristics of suspended-load-dominated hyperpycnal flows (Mulder et al., 2003; Zavala and Pan, 2018). In addition, sedimentary features of light layers (light gray silty clay) are similar with those of Holocene hemipelagic sediments. Such sedimentary characteristics could confirm our reasonable explanations of dark- and light-layer formation processes.

The aforementioned theoretical mechanism for lamina formation emphasizes pulsed sedimentation associated with mean high-water-line variations driven by the lunar nodal tide (Fig. 12). In fact, complicated characteristics of lamina occurrences and dark-layer thicknesses indicate that the cross-slope transport of coastal coarse sediments is influenced not only by the lunar nodal tide, but also by other factors, such as sea level, shelf topography, other sedimentary cycle, and event-driven sedimentation.

Core-estuary distance and topographic slope proxy (details in Fig. S6) were used to reflect the influence of sea level and shelf topography on the cross-slope transport of the coastal coarse sediments. Due to a large topographic slope (average 1.0 km/m), although sea level gradually rose from –135 to –115 m (Lambeck et al., 2014), the core-estuary distance was relatively short and stable (177–191 km) from 20.8 to 15.9 cal ka BP. In this period, large amounts of coastal coarse sediments were prone to be remobilized into the deep sea to form dark layers under the tidal influence. Accordingly, the laminar sediments were developed, and the thickness and occurrence frequency of dark layers were generally not affected by the rising sea level (Fig. S6). In addition, paleo-shoreline shape was harbor-shaped during this period, which could have an amplifying effect on the tidal intensity (Boyd et al., 1992). Due to a small topographic slope (average 13.3 km/m), gradually rising sea level (from –115 to –100 m) led to a progressively long core-estuary distance

(191–377 km) from 15.9 to 14.3 cal ka BP, resulting in gradually decreased amounts of the coastal sediments remobilized to the deep sea under the tidal influence. Accordingly, the thickness and frequency of dark layers gradually decreased from 15.9 to 15.1 cal ka BP (Fig. S6). From 15.1 to 14.3 cal ka BP, the unobvious laminar sediments were possibly related to the long distances (~370 km). The long core-estuary distances make it difficult for coastal coarse sediments to be remobilized to the deep sea under the lunar nodal tidal influence, finally resulting in undeveloped dark layers in the deep sea. In addition, unobvious laminar sediments from 16.5 to 16.2 cal ka BP show similar elemental-ratio variations with the unobvious laminar sediments from 15.1 to 14.3 cal ka BP, which might be related to the long distance (~370 km) triggered by unrecorded sea-level variations from 16.5 to 16.2 cal ka BP. At ~14.3 cal ka BP (corresponding to a 360-km core-estuary distance), one 2-cm thickness dark layer was developed, which could be related to a strong remobilization of coastal coarse sediments triggered by sea-level fluctuations in the meltwater pulse 1A. Since 14.3 cal ka BP, rapidly rising sea level combined with small topographic slopes has led to a rapidly long core-estuary distance (378–1,267 km), resulting in almost no coastal coarse sediments remobilized to the deep sea under the tidal influence (Fig. 12c). Accordingly, laminar sediments have been undeveloped in the deep sea since 14.3 cal ka BP. Therefore, under the combined influence of the sea level and topographic slope, the cross-slope transport of coastal coarse sediments developed when the core-estuary distance was less than 191 km. When the distance gradually increased from 191 to 370 km, the cross-slope transport gradually disappeared. When the distance was longer than 370 km, the cross-slope transport was undeveloped.

Other sedimentary cycle and event-driven sedimentation might also influence the cross-slope transport of the coastal coarse sediments during the last glacial 14.3–20.8 cal ka BP.

The periods of limina occurrences contain not only the lunar nodal tidal cycle, but also other cycles (Figs. 8–10). It is possible that other cycles can be interpreted as harmonic cycles of the perigee cycle and perigee eclipse cycle (Keeling and Whorf, 2000). Moreover, dark-layer occurrence frequency generally shows a fluctuation with the ~1.8-ka cycle (Fig. S6), which may be related to the 1.8-ka tidal cycle (Keeling and Whorf, 2000). Although sedimentary mechanisms of these tidal cycles are different, they would affect tidal intensity in different degree. Different tidal intensity implies different remobilization capacity, which would eventually lead to different thicknesses of coastal coarse sediments deposited in the deep sea. This might be one of reasons for a substantial variability in dark-layer thicknesses. Different dark-layer thickness might also be related to event-driven sedimentation. For example, 5–85 mm thickness coarse-grained layers (rich in Ca, Zr, and Si; depleted in K, Fe, and Ti) in Cores C0702 and DH6-1 in the East China Sea are related to storm-surge driven remobilization of coastal coarse sediments (Tian et al., 2019). Such sedimentary features of Cores C0702 and DH6-1 are similar with those of dark layers in Core MD05-2892. Therefore, the dark layers might be related to storm-surge driven remobilization of coastal coarse sediments. Modern climate data recorded that tropical cyclones were active in the southern South China Sea in winter (Shi et al., 2019). Accordingly, tropical cyclones may be active in this area during the last glaciation, resulting in a substantial variability in dark-layer thickness. Thus, different tidal cycles and storm-surge sedimentation might also influence the cross-slope transport of coastal coarse sediments during the last glacial 14.3–20.8 cal ka BP.

Although previous studies did not focus on the laminar sediments in the southern South China Sea, their core sediments contained several dark-layer sediments (e.g., Stattegger et al., 1997; Laj et al., 2005; Steinke et al., 2003; Zhao et al., 2011). During the last glacial

14.3–20.8 cal ka BP (estimated paleo-shoreline at –110 m water depth, Lambeck et al, 2014), dark-layer sediments were recorded at Cores SO18283 (–165 m water depth) and SO18284 (–226 m) in the shelf break (Stattegger et al., 1997; Steinke et al., 2003), at Cores SO18287 (–598 m) and SO18289 (–976 m) in the upper Sunda Slope (Stattegger et al., 1997; Steinke et al., 2003), at Cores MD05-2893 (–1,183 m), SO18268 (–1,975 m), and MD05-2895 (–1,982 m) in the lower Sunda Slope (Stattegger et al., 1997; Laj et al., 2005; Zhao et al., 2006, 2011; Jiwarungrueangkul et al., 2019). However, laminar sediments did not occur at Core SO18282 (–152 m) in the shallow shelf and at Core SO18294 (–849 m) in the seamount of the Sunda Slope during the same period (Stattegger et al., 1997; Steinke et al., 2003). By comparing other sediment records in the southern South China Sea, we found that laminar sediments during the last glacial 14.3–20.8 cal ka BP were mainly distributed from the shelf break to the lower Sunda Slope (corresponding to –165 to –1,982 m) and did not occur in the shallow shelf (<–165 m) or the seamounts. This not only indicated that laminar sediments were widespread, but also suggested that large amounts of shallow sediments were remobilized to the deep sea under the above factors including the long-term tidal cycle.

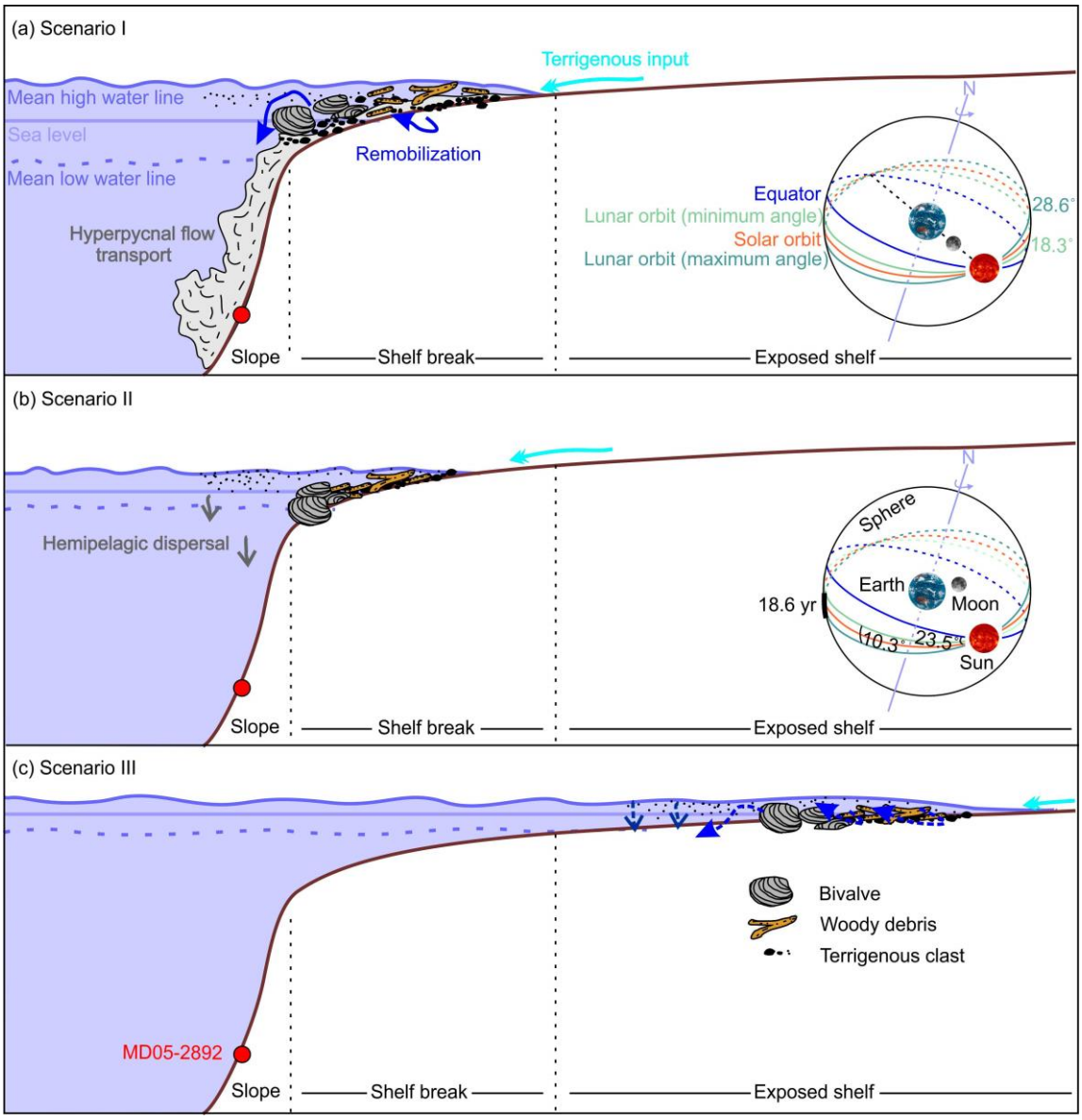

Fig. 12. Schematic scenarios showing lunar nodal tide-triggered cross-slope sediment transport in the southern South China Sea. (a) Scenario I: hyperpycnal flow transport of coarse-grained sediments triggered by strong tides during the last glacial sea-level lowstand. (b) Scenario II: hemipelagic dispersal of fine-grained sediments when the tidal intensity decreased during the last glacial sea-level lowstand. (c) Scenario III: limited sediment transport to the deep sea during the Holocene sea-level highstand. Schematic graphs of the Moon-Earth-Sun positions are shown for maximal tidal and weakened tidal intensity (a and b), respectively. The variation in angles of the lunar orbit with respect to the equator is also indicated (green; 18.3°–28.6°; Oost et al., 1993).

Although many factors could influence the cross-slope transport, our study presents that the lunar nodal tide could periodically trigger the cross-slope transport of the coastal

coarse sediments in the western Sunda Shelf during the last glacial sea-level lowstand, providing a new dynamic mechanism for sediment transport in the exposed shelf during the last glaciation. Exposed areas of global shelves are about 22.3×10^6 km^2 during the last glacial sea-level lowstand, of which ~40% are located near the equator (Wallmann, 2014; Wan et al., 2017, and references therein). During the last glaciation (and probably other glacial periods), these areas are characterized by a series of advantages including large lunar-nodal-tidal-cycle influence, abundant sediment supply and low sea-level position, providing ideal windows to further explore and test the mechanism proposed herein.

6. Conclusions

High-resolution XRF core-scanning elements combined with coarse-fraction observation on Core MD05-2892 in the southern South China Sea were used to reveal sedimentary features of laminae during the last glacial sea-level lowstand (14.3–20.8 cal ka BP) and the underlying cross-slope transport mechanism. We conclude that:

(1) The laminae show interbedded millimeter-scale dark and light layers. Dark layers are characterized by clayey silt that are relatively rich in Ca, Zr, Si, woody debris, quartz, and bivalve shell. Light layers are characterized by silty clay relatively rich in K, Ti, Fe, and clayey nodule. The dark and light layers respectively represent increased and reduced coarse-sediment supplies from the coastal zone in the western Sunda Shelf.

(2) Zr/K and Si/K ratios as well as grayness were used as proxies of lamina occurrences due to the differences in element compositions and colors between dark and light layers. Spectral analyses of these proxies show that the lamina occurrences have a persistent ~18.6-yr cycle, which is interpreted as the lunar nodal tidal cycle.

(3) The long-term tidal cycle in the laminar records is related to remobilization of coarse-grained sediments via mean high-water-line variations driven by the lunar nodal tide during the last glacial sea-level lowstand. The coarse-grained sediments were likely transported from the coastal shelf via the suspended-load-dominated hyperpycnal flow to the deep sea to form dark layers during periods of strengthened tidal intensity, while fine-grained sediments were dispersed via the hemipelagic transport to form light layers during periods of weakened tidal intensity.

Author contributions

Hongchao Zhao: Methodology, Software, Formal analysis, Investigation, Writing - Original Draft, Writing – Review & Editing. **Zhifei Liu**: Conceptualization, Methodology, Investigation, Resources, Writing – Review & Editing, Supervision, Funding acquisition. **Yulong Zhao, Jiawang Wu, and Christophe Colin**: Investigation, Writing – Review & Editing.

Declaration of competing interest

The authors declare that they have no known competing financial interests or personal relationships that could have appeared to influence the work reported in this paper.

Acknowledgments

We would like to thank the crew and scientists on board R/V *Marion Dufresne* for collecting the sediment core during the IMAGES XII/MARCO POLO cruise in 2005. We are also grateful to Xin Xie, Xiaofang Xu, Xibin Han, and Liangyu Wei for laboratory assistance in XRF core scanning, Xiaoying Jiang for laboratory assistance in oxygen isotope analysis, Kui Duan for assistance in designing Python codes, and David Black for

tidal tuning instructions. This work was financially supported by Shanghai Science and Technology Innovation Action Plan (20590780200) and National Natural Science Foundation of China (42130407, 42188102). Supplementary text and figures, data table of Core MD05-2892 generated by this study, and Python script of grayness extraction are provided as Supplementary Data in electronic formats.

References

Allen, J.R.L., 1981. Lower Cretaceous tides revealed by cross-bedding with mud drapes. Nature 289, 579–581. https://doi.org/10.1038/289579a0

Berger, W.H., Schimmelmann, A., Lange, C.B., 2004. Tidal cycles in the sediments of Santa Barbara Basin. Geology 32, 329–332. https://doi.org/10.1130/G20249.2

Blaauw, M., 2010. Methods and code for "classical" age-modelling of radiocarbon sequences. Quat. Geochronol. 5, 512–518. https://doi.org/10.1016/j.quageo.2010.01.002

Black, D.E., Hameed, S., Peterson, L.C., 2009. Long-term tidal cycle influences on a Late-Holocene clay mineralogy record from the Cariaco Basin. Earth Planet. Sci. Lett. 279, 139–146. https://doi.org/10.1016/j.epsl.2008.12.040

Boyd, R., Dalrymple, R., Zaitlin, B.A., 1992. Classification of clastic coastal depositional environments. Sediment. Geol. 80, 139–150. https://doi.org/10.1016/0037-0738(92)90037-R

Croudace, I.W., Rindby, A., Rothwell, R.G., 2006. Itrax: Description and evaluation of a new multi-function X-ray core scanner. In: Rothwell, R.G. (Ed.), New techniques in sediment core analysis. Geol. Soc., London, Spec. Publ. 267, 51–63.

De Boer, P.L., Alexandre, J.T., 2012. Orbitally forced sedimentary rhythms in the stratigraphic record: Is there room for tidal forcing? Sedimentology 59, 379–392. https://doi.org/10.1111/j.1365-3091.2011.01255.x

Gebregiorgis, D., Giosan, L., Hathorne, E.C., Anand, P., Nilsson-Kerr, K., Plass, A., Lückge, A., Clemens, S.C., Frank, M., 2020. What can we learn from X-ray fluorescence core scanning data? A paleomonsoon case study. Geochem. Geophys. Geosyst. 21, e2019GC008414. https://doi.org/10.1029/2019GC008414

Ghil, M., Allen, M.R., Dettinger, M.D., Ide, K., Kondrashov, D., Mann, M.E., Robertson, A.W., Saunders, A., Tian, Y., Varadi, F., Yiou, P., 2002. Advanced spectral methods for climatic time series. Rev. Geophys. 40, 1003. https://doi.org/10.1029/2000RG000092

Gratiot, N., Anthony, E.J., Gardel, A., Gaucherel, C., Proisy, C., Wells, J.T., 2008. Significant contribution of the 18.6 year tidal cycle to regional coastal changes. Nat. Geosci. 1, 169–172. https://doi.org/10.1038/ngeo127

Grinsted, A., Moore, J.C., Jevrejeva, S., 2004. Application of the cross wavelet transform and wavelet coherence to geophysical time series. Nonlinear Process. Geophys. 11, 561–566. https://doi.org/1607-7946/npg/2004-11-561

Hage, S., Cartigny, M.J.B., Sumner, E.J., Clare, M.A., Hughes Clarke, J.E., Talling, P.J., Lintern, D.G., Simmons, S.M., Silva Jacinto, R., Vellinga, A.J., Allin, J.R., Azpiroz-Zabala, M., Gales, J.A., Hizzett, J.L., Hunt, J.E., Mozzato, A., Parsons, D.R., Pope, E.L., Stacey, C.D., Symons, W.O., Vardy, M.E., Watts, C., 2019. Direct monitoring reveals initiation of turbidity currents from extremely dilute river plumes. Geophys. Res. Lett. 46, 11310–11320. https://doi.org/10.1029/2019GL084526

Hanebuth, T., Stattegger, K., Grootes, P.M., 2000. Rapid flooding of the Sunda Shelf: A late-glacial sea-level record. Science 288, 1033–1035. https://doi.org/10.1126/science.288.5468.1033

Hanebuth, T., Stattegger, K., Schimanski, A., Lüdmann, T., Wong, H.K., 2003. Late Pleistocene forced-regressive deposits on the Sunda Shelf (Southeast Asia). Mar. Geol. 199, 139–157. https://doi.org/10.1016/S0025-3227(03)00129-4

Hanebuth, T., Voris, H., Yokoyama, Y., Saito, Y., Okuno, J., 2011. Formation and fate of sedimentary depocentres on Southeast Asia's Sunda Shelf over the past sea-level cycle and biogeographic implications. Earth-Sci. Rev. 104, 92–110. https://doi.org/10.1016/j.earscirev.2010.09.006

Heaton, T.J., Köhler, P., Butzin, M., Bard, E., Reimer, R.W., Austin, W.E.N., Bronk Ramsey, C., Grootes, P.M., Hughen, K.A., Kromer, B., Reimer, P.J., Adkins, J., Burke, A., Cook, M.S., Olsen, J., Skinner, L.C., 2020. Marine20—The marine radiocarbon age calibration curve (0–55,000 cal BP). Radiocarbon 62, 779–820. https://doi.org/10.1017/RDC.2020.68

Hossain, M., Uzzaman, H., Saif, S., 2018. Bangla digital number plate recognition using template matching for higher accuracy and less time complexity. Int. J. Comput. Appl. 181, 15–21. https://doi.org/10.5120/ijca2018918140

Hsu, S.K., Kuo, J., Lo, C.L., Tsai, C.H., Doo, W. B., Ku, C.Y., Sibuet, J.C., 2008. Turbidity currents, submarine landslides and the 2006 Pingtung earthquake off SW Taiwan. Terr. Atmos. Ocean. Sci. 19, 767–772.

Huang, J., Jiang, F., Wan, S., Zhang, J., Li, A., Li, T., 2016. Terrigenous supplies variability over the past 22,000 yr in the southern South China Sea slope: Relation to sea level and monsoon rainfall changes. J. Asian Earth Sci. 117, 317–327. https://doi.org/10.1016/j.jseaes.2015.12.019

Huang, J., Wan, S., Li, A., Li, T., 2019. Two-phase structure of tropical hydroclimate during Heinrich Stadial 1 and its global implications. Quat. Sci. Rev. 222, 105900. https://doi.org/10.1016/j.quascirev.2019.105900

Jiwarungrueangkul, T., Liu, Z., 2021. East Asian monsoon and sea-level controls on clay mineral variations in the southern South China Sea since the Last Glacial Maximum. Quat. Int. 592, 1–11. https://doi.org/10.1016/j.quaint.2021.04.033

Jiwarungrueangkul, T., Liu, Z., Zhao, Y., 2019. Terrigenous sediment input responding to sea level change and East Asian monsoon evolution since the last deglaciation in the southern South China Sea. Glob. Planet. Change 174, 127–137. https://doi.org/10.1016/j.gloplacha.2019.01.011

Kaye, C.A., Stuckey, G.W., 1973. Nodal tidal cycle of 18.6 yr.: Its importance in sea-level curves of the east coast of the United States and its value in explaining long-term sea-level changes. Geology 1, 141–144.

Keeling, C.D., Whorf, T.P., 2000. The 1,800-year oceanic tidal cycle: A possible cause of rapid climate change. Proc. Natl. Acad. Sci. U. S. A. 97, 3814–3819. https://doi.org/10.1073/pnas.070047197

Kiefer, J., Karamperidou, C., 2019. High-resolution modeling of ENSO-induced precipitation in the tropical Andes: Implications for proxy interpretation. Paleoceanogr. Paleoclimatology 34, 217–236. https://doi.org/10.1029/2018PA003423

Laj, C., Wang, P., Balut, Y., 2005. MD147-Marco Polo Images XII Cruise Report. Institut Polaire Francais, pp. 3–11.

Lambeck, K., Rouby, H., Purcell, A., Sun, Y., Sambridge, M., 2014. Sea level and global ice volumes from the Last Glacial Maximum to the Holocene. Proc. Natl. Acad. Sci. U. S. A. 111, 15296–15303. https://doi.org/10.1073/pnas.1411762111

Lee, H., Galy, V., Feng, X., Ponton, C., Galy, A., France-Lanord, C., Feakins, S.J., 2019. Sustained wood burial in the Bengal Fan over the last 19 My. Proc. Natl. Acad. Sci. U. S. A. 116, 22518–22525. https://doi.org/10.1073/pnas.1913714116

Leithold, E.L., Hope, R.S., 1999. Deposition and modification of a flood layer on the northern California shelf: Lessons from and about the fate of terrestrial particulate organic carbon. Mar. Geol. 154, 183–195. https://doi.org/10.1016/S0025-3227(98)00112-1

Li, M., Hinnov, L., Kump, L., 2019. Acycle: Time-series analysis software for paleoclimate research and education. Comput. Geosci. 127, 12–22. https://doi.org/10.1016/j.cageo.2019.02.011

Lintern, D.G., Hill, P.R., Stacey, C., 2016. Powerful unconfined turbidity current captured by cabled observatory on the fraser river delta slope, British Columbia, Canada. Sedimentology 63, 1041–1064. https://doi.org/10.1111/sed.12262

Liu, J., Wang, Y., Yang, R., Hsu, R., Kao, S., Lin, H., Kuo, F., 2012. Cyclone-induced hyperpycnal turbidity currents in a submarine canyon. J. Geophys. Res.: Oceans 117, C04033. https://doi.org/10.1029/2011JC007630

Molengraaff, G.A.F., Weber, M., 1921. On the relation between the Pleistocene Glacial period and the origin of the Sunda Sea (Java and South China Sea), and its influence on the distribution of coral reefs and on the land and freshwater fauna. K. Ned. Akad. Wet., Proc. Ser. B: Phys. Sci. 23, 395–439.

Mulder, T., Syvitski, J., Migeon, S., Faugères, J., Savoye, B., 2003. Marine hyperpycnal flows: Initiation, behaviorand related deposits. A review. Mar. Pet. Geol. 20, 861–882. https://doi.org/10.1016/j.marpetgeo.2003.01.003

Nakajima, T., 2006. Hyperpycnites deposited 700 km away from river mouths in the central Japan Sea. J. Sediment. Res. 76, 60–73. https://doi.org/10.2110/jsr.2006.13

Ojala, A.E.K., Francus, P., Zolitschka, B., Besonen, M., Lamoureux, S.F., 2012. Characteristics of sedimentary varve chronologies – A review. Quat. Sci. Rev. 43, 45–60. https://doi.org/10.1016/j.quascirev.2012.04.006

Oost, A.P., de Haas, H., Ijnsen, F., van den Boogert, J.M., de Boer, P.L., 1993. The 18.6 yr nodal cycle and its impact on tidal sedimentation. Sediment. Geol. 87, 1–11. https://doi.org/10.1016/0037-0738(93)90032-Z

Padman, L., Howard, S.L., Orsi, A.H., Muench, R.D., 2009. Tides of the northwestern Ross Sea and their impact on dense outflows of Antarctic Bottom Water. Deep-Sea Res. II 56, 818–834. https://doi.org/10.1016/j.dsr2.2008.10.026

Pelejero, C., Kienast, M., Wang, L., Grimalt, J.O., 1999. The flooding of Sundaland during the last deglaciation: Imprints in hemipelagic sediments from the southern South China Sea. Earth Planet. Sci. Lett. 171, 661–671. https://doi.org/10.1016/S0012-821X(99)00178-8

Peng, D., Hill, E.M., Meltzner, A.J., Switzer, A.D., 2019. Tide gauge records show that the 18.61-year nodal tidal cycle can change high water levels by up to 30 cm. J. Geophys. Res.: Oceans 124, 736–749. https://doi.org/10.1029/2018JC014695

Pugh, T., 1987. Tides, surges and mean sea-level. John Wiley and Sons Ltd, New York, U. S. A., pp. 269–308.

Puig, P., Greenan, B.J.W., Li, M.Z., Prescott, R.H., Piper, D.J.W., 2013. Sediment transport processes at the head of Halibut Canyon, eastern Canada margin: An interplay between internal tides and dense shelf-water cascading. Mar. Geol. 341, 14–28. https://doi.org/10.1016/j.margeo.2013.05.004

Reimer, P.J., Austin, W.E.N., Bard, E., Bayliss, A., Blackwell, P.G., Bronk Ramsey, C., Butzin, M., Cheng, H., Edwards, R.L., Friedrich, M., Grootes, P.M., Guilderson, T.P., Hajdas, I., Heaton, T.J., Hogg, A.G., Hughen, K.A., Kromer, B., Manning, S.W.,

Muscheler, R., Palmer, J.G., Pearson, C., Van Der Plicht, J., Reimer, R.W., Richards, D.A., Scott, E.M., Southon, J.R., Turney, C.S.M., Wacker, L., Adolphi, F., Büntgen, U., Capano, M., Fahrni, S.M., Fogtmann-Schulz, A., Friedrich, R., Köhler, P., Kudsk, S., Miyake, F., Olsen, J., Reinig, F., Sakamoto, M., Sookdeo, A., Talamo, S., 2020. The Intcal20 Northern Hemisphere radiocarbon age calibration curve (0–55 cal kBP). Radiocarbon 62, 725–757. https://doi.org/10.1017/RDC.2020.41

Richter, T.O., Van Der Gaast, S., Koster, B., Vaars, A., Gieles, R., De Stigter, H.C., De Haas, H., Van Weering, T.C.E., 2006. The Avaatech XRF core scanner: Technical description and applications to NE Atlantic sediments. In: Rothwell, R.G. (Ed.), New techniques in sediment core analysis. Geol. Soc., London, Spec. Publ. 267, 39–50.

Sathiamurthy, E., Voris, H., 2006. Maps of Holocene sea-level transgression and submerged lakes on the Sunda Shelf. Nat. Hist. J. Chulalongkorn Univ. Supplement 2, 1–44.

Sang, P.N., Liu, Z., Colin, C., 2022. Chemical weathering of the Mekong River basin with implication for East Asian monsoon evolution during the late Quaternary: Marine sediment records in the southern South China Sea. Front. Earth Sci. 10, 885547. https://doi.org/10.3389/feart.2022.885547

Shanmugam, G., 2020. Gravity flows: Types, definitions, origins, identification markers, and problems. J. Indian Assoc. Sedimentol. 37, 61–90. https://doi.org/10.51710/jias.v37i2.117

Shi, J., Jin, Z., Liu, Q., Fan, T., Gao, Z., 2021. Sunspot cycles recorded in Eocene lacustrine fine-grained sedimentary rocks in the Bohai Bay Basin, eastern China. Glob. Planet. Change 205, 103614. https://doi.org/10.1016/j.gloplacha.2021.103614

Shi, Y., Du, Y., Chen, Z., Zhou, W., 2019. Occurrence and impacts of tropical cyclones over the southern South China Sea. Int. J. Climatol. 40, 4218–4227. https://doi.org/10.1002/joc.6454

Stattegger, K., Kuhnt, W., Wong, H.K., Buhring, C., Haft, C., Hanebuth, T., Kawamura, H., Kienast, M., Lorenc, S., Lotz, B., Ludmann, T., Lurati, M., Muhlhan, N., Paulsen, A.-M., Paulsen, J., Pracht, J., Putar-Roberts, A., Hung, N.Q., Richter, A., Salomon, B., Schimanski, A., Steinke, S., Szarek, R., Nhan, N. V., Weinelt, M., Winguth, C., 1997. Cruise Report Sonne 115 Sundaflut. Sequence stratigraphy, Late Pleistocene-Holocene sea level fluctuation and high resolution record of the post-Pleistocene transgression on the Sunda Shelf. Geologisch-Paläontologisches Institut und Museum Christian-Albrechts-Universität Kiel, Deutschland, pp. 1–214.

Staub, J., Gastaldo, R., 2003. Late Quaternary sedimentation and peat development in the Rajang River Delta, Sarawak, East Malaysia. In: Sidi, F.H., Nummedal, D., Imbert, P., Darman, H., Posamentier, H.W. (Eds.), Tropical deltas of Southeast Asia—Sedimentology, stratigraphy, and petroleum geology. Soc. Sediment. Geol., Tulsa, Spec. Publ. 76, 71–87.

Steinke, S., Hanebuth, T., Vogt, C., Stattegger, K., 2008. Sea level induced variations in clay mineral composition in the southwestern South China Sea over the past 17,000 yr. Mar. Geol. 250, 199–210. https://doi.org/10.1016/j.margeo.2008.01.005

Steinke, S., Kienast, M., Hanebuth, T., 2003. On the significance of sea-level variations and shelf paleo-morphology in governing sedimentation in the southern South China Sea during the last deglaciation. Mar. Geol. 201, 179–206. https://doi.org/10.1016/S0025-3227(03)00216-0

Stuiver, M., Reimer, P.J., 1993. Extened ^{14}C data base and revised CALIB 3.0 ^{14}C age calibration program. Radiocarbon 35, 215–230. https://doi.org/10.1017/S0033822200013904

Ta, T.K.O., Nguyen, V.L., Tateishi, M., Kobayashi, I., Tanabe, S., Saito, Y., 2002. Holocene delta evolution and sediment discharge of the Mekong River, southern Vietnam. Quat. Sci. Rev. 21, 1807–1819. https://doi.org/10.1016/S0277-3791(02)00007-0

Tian, Y., Fan, D., Zhang, X., Chen, B., Wang, L., Liu, M., Yang, Z., 2019. Event deposits of intense typhoons in the muddy wedge of the East China Sea over the past 150 years. Mar. Geol. 410, 109–121. https://doi.org/10.1016/j.margeo.2018.12.010

Tjallingii, R., Röhl, U., Kölling, M., Bickert, T., 2007. Influence of the water content on X-ray fluorescence core-scanning measurements in soft marine sediments. Geochem. Geophys. Geosyst. 8, Q02004 . https://doi.org/10.1029/2006GC001393

Tomkratoke, S., Sirisup, S., Udomchoke, V., Kanasut, J., 2015. Influence of resonance on tide and storm surge in the Gulf of Thailand. Cont. Shelf Res. 109, 112–126. https://doi.org/10.1016/j.csr.2015.09.006

Voris, H.K., 2000. Maps of Pleistocene sea levels in Southeast Asia: Shorelines, river systems and time durations. J. Biogeogr. 27, 1153–1167. https://doi.org/10.1046/j.1365-2699.2000.00489.x

Wallmann, K., 2014. Is late Quaternary climate change governed by self-sustained oscillations in atmospheric CO_2? Geochim. Cosmochim. Acta 132, 413–439. https://doi.org/10.1016/j.gca.2013.10.046

Wan, S., Clift, P.D., Zhao, D., Hovius, N., Munhoven, G., France-Lanord, C., Wang, Y., Xiong, Z., Huang, J., Yu, Z., Zhang, J., Ma, W., Zhang, G., Li, A., Li, T., 2017. Enhanced silicate weathering of tropical shelf sediments exposed during glacial

lowstands: A sink for atmospheric CO_2. Geochim. Cosmochim. Acta 200, 123–144. https://doi.org/10.1016/j.gca.2016.12.010

Wu, J., Liu, Z., Zhou, C., 2013. Provenance and supply of Fe-enriched terrigenous sediments in the western equatorial Pacific and their relation to precipitation variations during the late Quaternary. Glob. Planet. Change 108, 56–71. https://doi.org/10.1016/j.gloplacha.2013.06.002

Xie, X., Zheng, H.B., Qiao, P.J., 2014. Millennial climate changes since MIS 3 revealed by element records in deep-sea sediments from northern South China Sea. Chin. Sci. Bull. 59, 776–784. https://doi.org/10.1007/s11434-014-0117-9

Zavala, C., Pan, S., 2018. Hyperpycnal flows and hyperpycnites: Origin and distinctive characteristics. Lithol. Reserv. 30, 1–27. https://doi.org/10.3969/j.issn.1673-8926.2018.01.001

Zhang, Y., Liu, Z., Zhao, Y., Colin, C., Zhang, X., Wang, M., Zhao, S., Kneller, B., 2018. Long-term in situ observations on typhoon-triggered turbidity currents in the deep sea. Geology 46, 675–678. https://doi.org/10.1130/G45178.1

Zhao, Y., Liu, Z., Cheng, X., Jian, Z., 2006. Dominance factors of the terrigenous sediment granulometric distribution in the lower Sunda Slope. Mar. Geol. Quat. Geol. 26, 73–78 (in Chinese with English abstract).

Zhao, Y.L., Liu, Z.F., Colin, C., Xie, X., Wu, Q., 2011. Turbidite deposition in the southern South China Sea during the last glacial: Evidence from grain-size and major elements records. Chin. Sci. Bull. 56, 3558–3565. https://doi.org/10.1007/s11434-011-4685-7